



OPEN ACCESS

EDITED BY

Glen T. Snyder,
The University of Tokyo, Japan

REVIEWED BY

Renat Shakirov,
V.I. Il'ichev Pacific Oceanological Institute
(RAS), Russia
Pawan Dewangan,
Council of Scientific and Industrial
Research (CSIR), India

*CORRESPONDENCE

Nancy G. Prouty,
✉ nprouty@usgs.gov

RECEIVED 13 April 2023

ACCEPTED 31 July 2023

PUBLISHED 10 August 2023

CITATION

Rudebusch JA, Prouty NG, Conrad JE,
Watt JT, Kluesner JW, Hill JC, Miller NC,
Watson SJ and Hillman JIT (2023), Diving
deeper into seep distribution along the
Cascadia convergent
margin, United States.
Front. Earth Sci. 11:1205211.
doi: 10.3389/feart.2023.1205211

COPYRIGHT

© 2023 Rudebusch, Prouty, Conrad,
Watt, Kluesner, Hill, Miller, Watson and
Hillman. This is an open-access article
distributed under the terms of the
[Creative Commons Attribution License
\(CC BY\)](https://creativecommons.org/licenses/by/4.0/). The use, distribution or
reproduction in other forums is
permitted, provided the original author(s)
and the copyright owner(s) are credited
and that the original publication in this
journal is cited, in accordance with
accepted academic practice. No use,
distribution or reproduction is permitted
which does not comply with these terms.

Diving deeper into seep distribution along the Cascadia convergent margin, United States

Jane A. Rudebusch¹, Nancy G. Prouty^{1*}, James E. Conrad¹,
Janet T. Watt¹, Jared W. Kluesner¹, Jenna C. Hill¹,
Nathaniel C. Miller², Sally J. Watson^{3,4} and Jess I. T. Hillman⁵

¹United States Geological Survey, Pacific Coastal and Marine Science Center, Santa Cruz, CA, United States, ²United States Geological Survey, Woods Hole Coastal and Marine Science Center, Woods Hole, MA, United States, ³National Institute of Water and Atmospheric Research (NIWA), Wellington, New Zealand, ⁴Institute of Marine Science, University of Auckland, Auckland, New Zealand, ⁵GNS Science, Lower Hutt, New Zealand

Previous margin-wide studies of methane seep distribution along the Cascadia Subduction Zone indicate peaks in seep density within the landward limit of the of gas hydrate stability zone (GHSZ; ≤ 500 m depth), suggesting a link between current ocean warming, acceleration of hydrate dissociation, and methane emissions. This inferred connection, however, may not account for regional geologic and/or structural complexities driving methane seepage. Expanding upon an existing seep database by adding new seep data, we conducted statistical and spatial analyses to determine margin-wide distribution trends and offer a tectonic framework for understanding the tendency toward non-normality and spatial clustering. We then highlight the role of local-scale drivers of seep formation in addition to the first-order tectonic framework, using systematic geologic/geomorphic characterization of seep emission sites in southern Cascadia and case studies using meta-attribute analysis of seismic reflection data. Seep distribution along the margin is non-random, but instead of clustering along the 500-m isobath, regions of high seep density occur in canyons and topographic highs. New findings from this study conclude that co-location of the outer arc high (OAH) and the landward limit of the GHSZ may explain high concentrations of seeps where deformation is the greatest and hydrates are unstable. Detailed analysis of the spatial relationships between seep sites and geologic-geomorphic features in southern Cascadia reveal a link between seeps and anticlines, with 52% of the seeps found in association with anticlines, 36% found at faults, 16% associated with canyons, and 11% at seafloor failure scarps. Given that a majority of anticlines are located along or seaward of the OAH in the actively deforming outer wedge, we suggest that the location of the OAH is a primary structural control on seep distribution. This scenario is supported by neural network analysis of multichannel seismic data revealing zones of probable fluid migration along vertical pipes, faults, and chimneys in the vicinity of active seep sites on anticlines. Determining linkages between seeps and submarine tectonic geomorphology is a crucial first step for understanding and forecasting the distribution of methane seepage, but also a necessity for evaluating causal relationships between ocean warming and gas hydrate stability.

KEYWORDS

methane plume, cold seep, hydrate, Cascadia, fluid-trapping, gas chimney

1 Introduction

Warming of ocean-bottom waters has been linked to hydrate dissociation at the landward limit of the gas hydrate stability zone (GHSZ) in the Southern Ocean (Ketzer et al., 2020) and Arctic Ocean (Westbrook et al., 2009; Berndt et al., 2014), and has been suggested as a mechanism to explain the high frequency of seep emissions along the 500-m isobath off the Oregon and Washington coasts (Hautala et al., 2014; Johnson et al., 2015). For example, Merle et al. (2021) reported a nearly bell-shaped normal distribution curve in the depth-frequency of over 1,300 emission sites along the Washington and northern/central Oregon margin that correlates with the landward limit of the GHSZ, suggesting a link between methane release and ocean warming. Emissions of hydrogen sulfide, methane, and other hydrocarbon-rich fluids into the sediment and water column are well documented and widespread along the Cascadia margin (e.g., Johnson et al., 2015; Riedel et al., 2018; Merle et al., 2021), with precipitates of slow growing methane-derived authigenic carbonates suggesting fluid seepage over thousands of years (Bohrmann et al., 1998; Suess et al., 1999; Teichert et al., 2003; Torres et al., 2009; Johnson et al., 2015; Paull et al., 2015). In addition, the occurrence of bottom simulating reflectors (BSRs), the boundary between hydrate-containing sediment overlying sediment that contains free gas (Trehu et al., 1995), over large areas suggests a high abundance of hydrates and trapped free gas below along the Cascadia margin accretionary complex (Tréhu et al., 2004; Torres et al., 2009). Gas hydrates are stable over moderate-pressure (P) conditions and a range of low temperatures (T) found close to the seafloor at deepwater continental slopes sites with sufficient methane saturation (Canfield et al., 2005; Collett, 2009). Changes to the P-T stability conditions, such as ocean warming, can drive the breakdown (e.g., dissociation) of hydrates (see review by Ruppel and Waite, 2020). However, these temporal processes are superimposed on long-lived geologic controls of fluid migration that define seep characteristics and help explain the driving mechanisms of fluid expulsion (Judd and Hovland, 2007; Suess, 2014). Therefore, a detailed geospatial analysis of seep distribution, including newly acquired data from southern Cascadia, is needed in order to determine if there is a link between current ocean warming and seep distribution along the Cascadia margin.

To address this knowledge gap and further explore geologic controls on focused seep distribution along the Cascadia margin, we examine new water-column data from U.S. Geological Survey (USGS) seafloor mapping activities on the National Oceanic and Atmospheric Administration (NOAA) Hydrographic Survey Vessels *Rainier* and *Fairweather* from 2018 to 2021, as well as from both active and relict (or dormant) seep indicators such as authigenic carbonates and microbial mats to supplement the existing seep composite database (Merle et al., 2021). To develop a tectonic framework of seep emissions based on geologic controls, along-margin variation in seep distribution is investigated in the context of morphotectonic regions and seismogenic behavior. In particular, we integrate new multibeam bathymetry, backscatter data, and seismic reflection profiles in southern Cascadia to

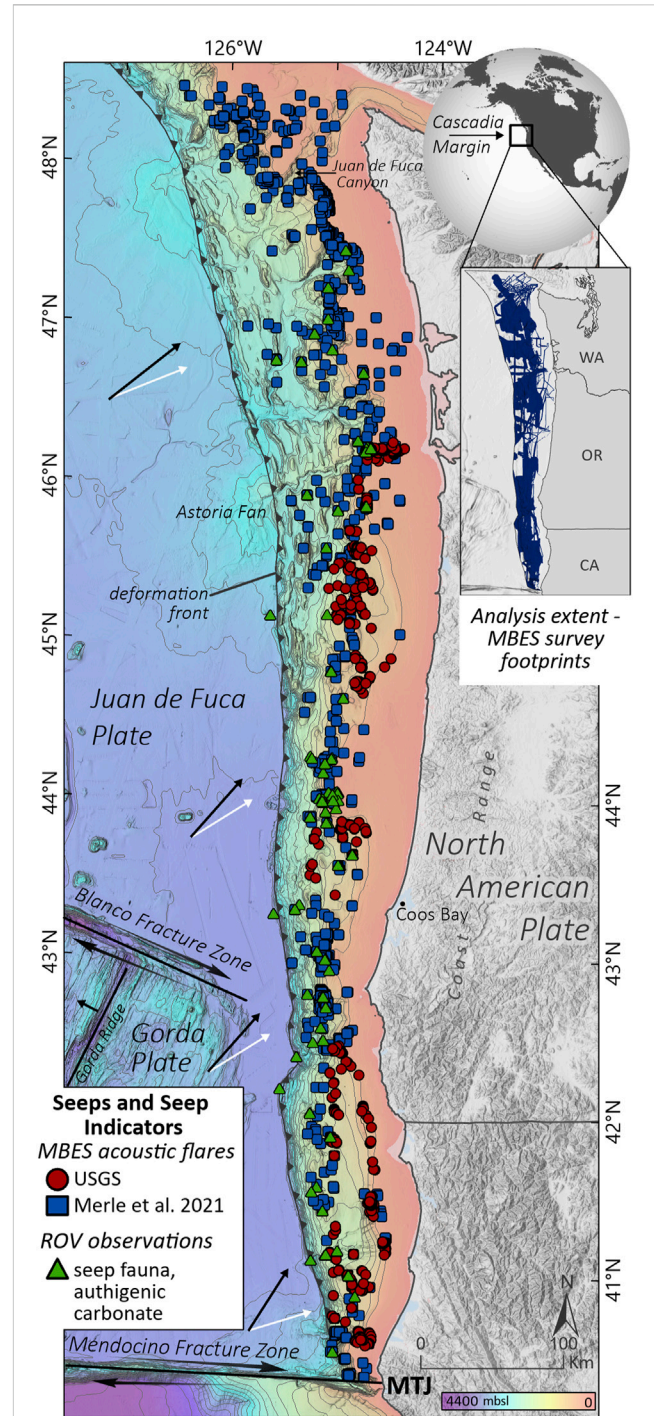


FIGURE 1
Regional overview map of the Cascadia convergent margin with the locations of seeps according to the data reference source. Inset shows the extents of the multibeam sonar surveys from which seep data were derived and that was used as a bounding polygon of the analysis extent. Topo-bathymetry is from Ryan et al. (2009). Black arrows indicate relative plate between the Juan de Fuca and Gorda plates and North America (DeMets et al., 2010); white arrows, relative plate motions between the Juan de Fuca and Gorda plates and Oregon Coast Range (Wells et al., 2002; McCaffrey et al., 2007). Isobaths (gray contour lines) are set at 200 m depth intervals from zero.

determine potential controls on focused fluid flow in an area with previously sparse coverage. With this updated composite dataset, we examine regional variation in the depth distribution of methane seeps along the Cascadia margin and test our hypothesis that seep distribution is fundamentally tied to first- and second-order geological phenomena that operate independently of gas hydrate dissociation in response to contemporary ocean warming.

1.1 Geologic setting

The Cascadia Subduction Zone (CSZ) is an active plate boundary where the Juan de Fuca, Gorda, and Explorer plates subduct beneath the North American plate. This convergent boundary extends over 1,300 km from the Nootka fracture zone offshore British Columbia (Canada) in the north (Audet et al., 2008) to the Mendocino triple junction offshore northern California (United States) in the south (Figure 1). A large accretionary wedge composed of both terrigenous and marine sediments has been accreted to the North America plate along the CSZ. This wedge contains a series of folded and thrust ridges striking subparallel to the continental slope that form large anticlines (Cochrane and Lewis, 1984; Goldfinger et al., 1991). There is also significant along-strike geophysical and geologic heterogeneity that has been linked to different modes and rates of stress accumulation and release along the margin (see summary in Walton et al., 2021). Such variability could reflect differences in sediment and pore-fluid properties that ultimately influence fluid migration due to rapid compaction and dewatering rates (Tréhu et al., 2004; Han et al., 2017). For example, high glacial sediment flux during the Pleistocene significantly expanded the size of the outer wedge in northern Cascadia, between Juan de Fuca and Astoria Canyons (Silver, 1972; Barnard, 1973).

Broadly, the offshore accretionary wedge can be divided into two margin-parallel zones separated by the outer arc high (OAH), which is defined as a broad structural high that bounds the seaward edge of the shelf forearc basins (e.g., von Huene and Scholl, 1991; Clift and Vannucchi, 2004; McNeill and Henstock, 2014). While the OAH typically follows the shelf break along the 200-m isobath in Cascadia, deviations from the shelf break, both landward and seaward are observed, and may be linked to regional variations in the width of the outer wedge. Watt and Brothers (2020) identified four distinct morphotectonic regions based on careful examination of geophysical examination of seismic profiles to describe variable accretionary wedge width, shape, and structural vergence. These four regions include: (1) Vancouver Island, British Columbia, Canada (average width, linear wedge, seaward and mixed vergence); (2) Washington, United States (higher width, concave wedge, landward and mixed vergence); (3) northern and central Oregon, United States (average width, linear and convex wedge, mixed and seaward vergence); and (4) southern Oregon and northern California, United States (lower width, convex wedge, seaward and mixed vergence). Regional patterns and differences in the tectonic evolution of the outer accretionary wedge are also linked to Cascadia margin-wide heterogeneity in the distribution and character of the BSR (Tréhu and Phrampus, 2022). For example, BSRs were observed beneath anticlines where internal deformation of the wedge replenishes the supply of methane to the GHSZ at the

crest of the anticlines by compacting sediments and providing pathways to the shallow subsurface (Tréhu and Phrampus, 2022). Therefore, tectonic factors influencing the occurrence and disruption of the BSR and associated fluid expulsion are also important in constraining the spatial distribution of cold seeps along the Cascadia margin.

2 Data and methods

2.1 Seafloor mapping and seep database

The seep database includes previously published data documenting over 2,850 active seep flares on the seafloor using ship-based multibeam echo-sounding (MBES) sonar (Johnson et al., 2015; Riedel et al., 2018; Merle et al., 2021), and 902 new seep flares identified during surveys by the NOAA Ships *Rainier* in 2018 (surveys H13117, H13118, H13119, H13137, and H13206) and *Fairweather* in 2019 and 2021 (surveys W00474, W00475, and H13549) (Conrad and Rudebusch, 2023; Supplementary Table S1). Bubble plumes associated with seeps were mapped in the MBES water column backscatter data using QPS FMMidwater software, using techniques and identification criteria similar to those described by Merle et al. (2021). The geologic setting of the bubble plume locations was determined from interpretation of the morphologic and bottom characteristics of the seafloor from multibeam bathymetry and backscatter data (<https://www.ncei.noaa.gov/maps/bathymetry/>) and from subbottom data derived from seismic reflection profiles (Balster-Gee et al., 2023a). In addition, evidence for both active and relict (or dormant) seep indicators including authigenic carbonates, vesicomid clams, tubeworms, and microbial mats, were included from seafloor observations and collections made using remotely operated vehicles (ROVs) (Supplementary Table S1). The inclusion of seep evidence from ROVs proved useful for revealing additional seep locations that were not detected by traditional ship hull-mounted multibeam echosounders. Therefore, seep-distribution reported here is a presence-pseudoabsence dataset, not presence-absence. Diffuse seepage, where gas concentrations are not sufficient for gas phase emissions, was not included given the difficulty in identifying diffuse seepage acoustically. Following previously published methods of Johnson et al. (2015) for removing possible double-counted seeps due to overlapping surveys, we aggregated seeps found within 300 m of each other into single seep “emission site,” yielding a dataset of 880 seep emission sites for a new composite database (Supplementary Table S1). To account for variance in surface area of the depth contour polygons and the effect of unequal survey effort across depth bins, we included only seeps detected via MBES so that we could normalize the number of seeps with the corresponding area mapped and determine seep density.

2.2 Statistical analysis

Survey footprints derived from the bathymetry of the corresponding MBES surveys used to acquire seep locations were loaded into a GIS and merged into a single polygon layer. This layer

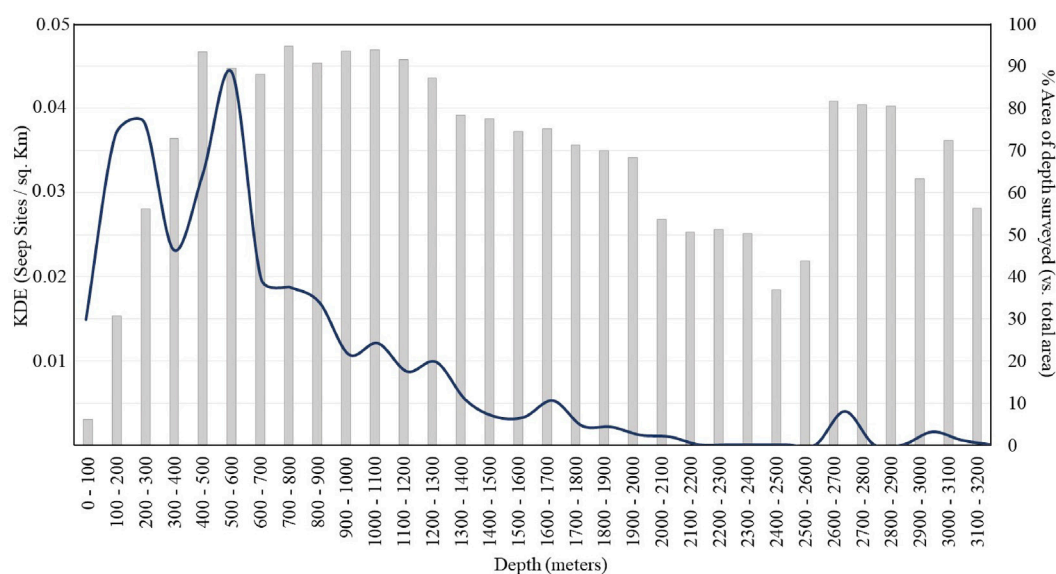


FIGURE 2

Kernel density estimation (KDE) of seeps (blue line) calculated as the number of emission sites per square kilometer of MBES-surveyed area in 100-m interval depth bins overlaid on the percentage of the seafloor mapped (gray bars) with MBES and co-located water-column data for each depth bin, as compared with the total area of the depth contour (area mapped/total area). Depths with values close to 100 signify near-complete survey coverage, whereas values close to 0 represent data deficiencies with regards to sparse MBES and water-column survey coverage.

was then used as a mask to extract a continuous 100-m resolution depth surface from a global multiresolution bathymetric elevation model (Ryan et al., 2009), representing the area mapped corresponding with the seep location data. Depth contour polygons were created from this layer at 100-m intervals and seep emission sites were spatially joined to their respective depth contour polygon. Seep density (per sq. kilometer) was calculated for each 100-m depth contour. A smoothed kernel density estimation curve was fitted to the data for the margin-wide (Figure 2), as well as at the regional scale (Figure 3), in order to investigate seep distribution per morphotectonic region. To test for normality in the seep depth distribution we used normal Q-Q plots and a Shapiro-Wilk test (Shapiro and Wilk, 1965; Wilk and Gnanadesikan, 1968). Patterns in seep distribution were further explored in order to identify significant seep clusters along the margin (Optimized Hot Spot Analysis tool in ArcGIS Pro 3.0, Esri). Optimized Hot Spot Analysis was used to spatially interrogate the dataset to optimally aggregate coincident features into hexbins based on the Global Moran's I statistic of spatial autocorrelation, and then calculate a Getis-Ord G_i^* statistic for each hexbin to compare the aggregated counts of seeps within each hexbin against those of its nearest neighbors. Cluster predictions are determined by the aggregation of seeps within neighboring hexbins as compared to the null hypothesis of a random distribution. We used an analysis cell size of 10 km and a fixed distance band of 20 km, as determined by the initial steps run by the Optimized Hot Spot Analysis tool to identify the optimal scale of analysis. All aggregation hexbins had a minimum of 8 neighbors, and on average 16 nearest neighbors were used with a moving window analysis to determine statistical clusters. The resultant z-scores for each aggregation hexbin identified the intensity of the clustering, with larger positive z-scores (p -value < 0.05) indicating more significant seep clusters. We

included only the clustering for features significant at the 95%–99% confidence levels.

2.3 Geologic-geomorphic attribute

In order to determine potential controls on focused fluid flow in southern Cascadia, an area with previously sparse coverage, we systematically assigned a primary (and in some cases, secondary) geologic/geomorphic attribute to each seep emission site in region 4 of Watt and Brothers (2020) Seafloor expressions of fluid expulsion or other indicators of fluid flow, such as pockmarks or authigenic carbonates but otherwise lacking evidence of active seepage, were not included. Instead, we integrated new multibeam bathymetry, backscatter data, and seismic reflection profiles to identify attributes previously inferred to be associated with substrate fluid flow: anticline, fault, failure scarp, shelfbreak, channel, bedding outcrop, and canyon (e.g., Skarke et al., 2014; Crutchley et al., 2018; Riedel et al., 2018; Prouty et al., 2020). Locations of these attributes were determined from their geomorphic expression on the seafloor (Supplementary Figure S1) and supplemented with seismic reflection profiles where available. For example, bubble plume locations were combined with the multibeam bathymetry and backscatter data (<https://www.ncei.noaa.gov/maps/bathymetry/>) and seismic reflection profiles (Triezenberg et al., 2016) for visualization and interpretation of the local geologic/geomorphic setting within a 50-m buffer of the seep occurrences and logged using a geographic information system (GIS) (ArcMap 10, Esri). Information on anticline locations was derived from previously published neotectonic maps in southern Cascadia (Clarke and Carver, 1992; Goldfinger et al., 1992; Goldfinger et al., 1997) but is currently unavailable for northern Cascadia.

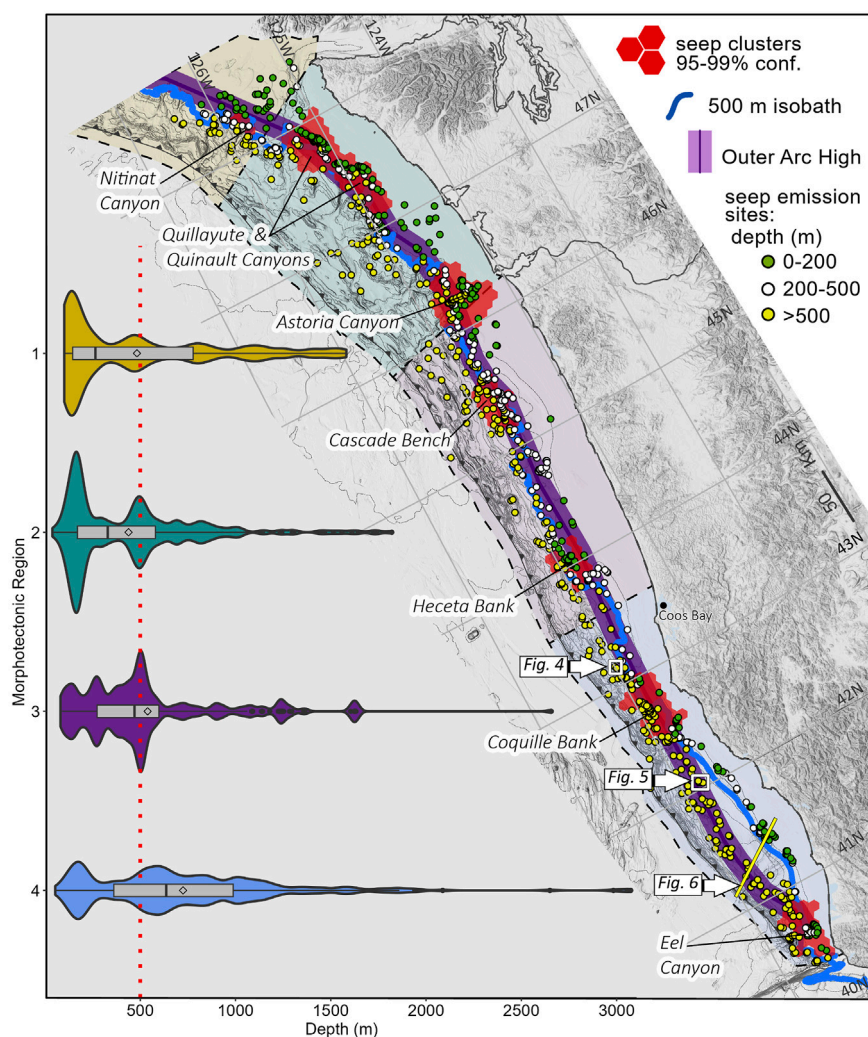


FIGURE 3

(right) Locations of the seven seep clusters (red) identified in Cascadia, and their spatial relationships with the landward limit of the gas hydrate stability zone (blue contour line), the outer arc high (purple shaded region) as defined in [Watt and Brothers \(2020\)](#) and significant associated submarine canyons or structural highs. Seep emission sites (circles) color coded by depth bin (0–200 green; 200–500 white; >500 yellow). Location for [Figures 4, 5](#) and seismic line for [Figure 6](#) (yellow line) are shown (left). Variability in seep depth distributions according to morphotectonic region ([Watt and Brothers, 2020](#)) as shown with violin plots inset with box plots. Violin plots show a kernel density estimation curve representing the probability of occurrence of seep emission sites at a given depth. Box-and-whisker plots display five-number summary statistics of seep depth, with both median (vertical line) and mean (diamond) depth values displayed inside the boxes. The landward limit of the gas hydrate stability zone for the Cascadia margin is indicated with the red dashed lines (500-m isobath).

In addition to examining seep distribution in the context of regional controls in southern Cascadia, margin-wide seep distribution was evaluated with respect to the landward limit of the GHSZ and the OAH. The OAH was designated as the location of broad structural high with a ± 10 -km buffer that runs along the seaward edge of the shelf forearc basins ([Watt and Brothers, 2020](#)). [Joung et al. \(2022\)](#) showed the landward limit of gas hydrate determined for the northern Cascadia margin based on bottom water temperatures recorded by CTD data. This type of analysis is hard to adapt for the whole margin due to lack of complete data coverage (C.D. Ruppel, USGS, written commun., 07/04/23) and we instead adopted the 500-m isobath as the nominal the landward limit of the GHSZ ([Tréhu and Phrampus, 2022](#)).

2.4 Seismic reflection data

Multichannel seismic reflection datasets were utilized to reveal subsurface structure and stratigraphy under mapped seeps where available (e.g., [Triezenberg et al., 2016](#)). Additional seismic surveys were collected in 2018 aboard the R/V *Coral Sea* using an 88-channel Geometrics GeoEel digital hydrophone streamer and Applied Acoustic Delta Sparker sound source ([Balster-Gee et al., 2023a](#)) and in 2019 onboard the R/V *Rachel Carson* and utilized a 72-channel Geometrics GeoEel streamer and the Delta Sparker sound source ([Balster-Gee et al., 2023b](#)). Both sparker datasets were processed following processing procedures laid out in [Kluesner et al. \(2019\)](#) and included SEG-D to SEG-Y conversion, geometry

correction, UTM conversion, common mid-point (cmp) binning, FK filter, spike removal, bandpass filtering, velocity analysis, normal move-out correction, trim static corrections, cmp stacking, post-stack migration, gap deconvolution, water column mute, and automatic gain control. In addition to the workflow above, the 2019 sparker dataset included prestack deterministic deconvolution using shot-to-shot source signature information recorded during acquisition.

2.5 Chimney analysis

To optimize the detection of gas and fluid migration pathways in the vicinity of active seep sites with focused fluid flow (Heggland, 2005; Ligtenberg, 2005; Kluesner et al., 2013; Brothers et al., 2014; Connolly, 2015), a fully connected multi-layer perceptron neural-network approach was applied to 2-D high-resolution multichannel seismic (MCS) profiles at seep sites in region 4. Within the OpendTect software package, twenty-one attributes were used as input nodes into the supervised neural-network chimney calculation, and each node was weighted during the neural-network training (for details see Kluesner and Brothers (2016)). The chimney meta-attribute results were projected onto seismic cross-sections using a gradational color scale with transparency that reveals only the highest (~80% and above) chimney probabilities, yielding a measurement of the probability between 0 (lowest) to 1 (highest) for presence of a chimney structure. Two types of features were identified, zones of probable fluid migration (e.g., vertical pipes, faults, and chimneys) and gassy sediments. The frequency-dependent reflectivity of gassy sediments due to scattering and absorption has been previously documented (e.g., Wood et al., 2008). The chimney meta-attribute analysis described above therefore represents a powerful method to discern subtle patterns of gas-related attenuation and their spatial relationships with the surrounding structure and stratigraphy in areas of focused fluid flow (Kluesner and Brothers, 2016; Prouty et al., 2020).

2.6 Methane-derived authigenic carbonates

Powdered carbonate samples for stable carbon ($\delta^{13}\text{C}$) and oxygen ($\delta^{18}\text{O}$) isotopic analysis were collected using a hand-held pneumatic drill to sample various components of authigenic carbonates collected along the Cascadia margin as a proxy for potential fluid sources. Isotopic composition was determined via ThermoScientific Kiel IV carbonate device interfaced to ThermoScientific MAT-253 dual-inlet isotope ratio mass spectrometer (IRMS) at the University of California, Santa Cruz, Stable Isotope Laboratory. Stable isotope values are reported in per mil (‰) relative to the international reference Pee Dee Belemnite (PDB). Analytical uncertainties (1σ) are 0.05‰ for $\delta^{13}\text{C}$ and 0.10‰ for $\delta^{18}\text{O}$. Mineralogy was determined by X-ray diffraction (XRD) using a Philips XRD with graphite monochromator at 40 kV and 45 mA as described in Prouty et al. (2016). Step scans were run from 5° to $65^\circ 2\theta$ with 0.02° steps, using CuK α radiation and a count time of 2 s per step following Hein et al. (2013). XRD digital scan data were analyzed using the Philips X'Pert High Score search-and-match function to identify minerals. The XRD 100 intensity

TABLE 1 Number of seep emission sites and summary statistics of seep depth (m) including depth range, median depth, first and third interquartile, and interquartile range (IQR) per morphotectonic region as defined in Watt and Brothers (2020).

	Morphotectonic region			
	1 <i>n</i> =77	2 <i>n</i> =275	3 <i>n</i> =250	4 <i>n</i> =278
Minimum depth	101	39	81	54
1st Quartile	145	170	274	361
Median	264	329	470	636
3rd Quartile	777	579	598	989
Maximum depth	1,581	1,820	2,656	3,074
IQR	632	409	324	626

peaks at 20 for calcite: 29.4, dolomite: 30.8, quartz: 26.6, and aragonite: 26.2 in order to determine major (>25%) carbonate phase. Results from new analysis were combined with previously published results from Cascadia (Torres et al., 2009).

3 Results

3.1 Margin-wide and regional seep distribution

Margin-wide seep depth distribution is shown in Figure 2, based on results from the smoothed density estimation curve of seep sites per 100 m depth intervals overlaid on the relative percent-area surveyed of each depth contour (Table 1). The MBES survey coverage varies with depth and is lowest in the very shallow water on the continental shelf from 0 to 200 m, where the narrowing of the swath width makes collecting large surface areas exceedingly difficult for the typical MBES systems. In most other depth bins, however, coverage is between 60%–95%. The margin-wide seep depth distribution is left-skewed with bimodal peaks at 200–300 m and 500–600 m and long-tailed showing numerous observations of deep seeps up to 3,100 m. Non-normality of the distribution was confirmed using normal Q-Q plots, which show significant deviation of the sample points from the linear model especially in the lower and upper quantiles, and a Shapiro-Wilk test ($W=0.5457$, p -value<0.05; Supplementary Figure S2).

Given that margin-wide plots of seep depth distribution can mask along-margin variation in seep depth trends, we evaluated the depth distribution of the seep emission sites within four morphotectonic regions of the Cascadia margin (Watt and Brothers, 2020). The depth-distribution of each of the four morphotectonic regions shows considerable variation (Figure 3), especially compared to the margin-wide depth distribution (Figure 2). In addition to displaying the median and quartiles (i.e., inset box-and-whisker plots), the violin plots use a kernel density estimation to show the distribution shape of the data (i.e., position and relative amplitude) and probability of seep distribution along the depth range (Table 1). In regions 1 and 2,

39%–42% of seeps are found on shallow continental shelf (0–200 m), with 23%–26% on the upper slope and landward limit of the GHSZ (200–500 m), and 35% found in deeper waters and within the GHSZ (>500 m) (Figure 3). In region 3, 42% are located on the upper slope up to the landward limit of GHSZ, characterized by an interquartile range of 300–600 m, but equally 42% are found within the GHSZ, and a smaller portion on the shelf (15%). In contrast, seeps in region 4 were found in deeper water, such that 68% of the seeps are within the GHSZ (interquartile range = 600–1,000 m), 15% on the upper slope and landward limit GHSZ, and the remaining 17% on the shelf. In summary, only the median seep depth in region 3 coincides with the depth range of the landward limit GHSZ. The probability of seeps occurring within the depth range of the landward limit GHSZ is only valid in region 3. In contrast, the median seep depth in regions 1 and 2 are shallower with respect to the landward limit of the GHSZ and deeper in region 4, suggesting a margin-wide seep distribution trend toward deeper water southward along the margin (Figure 3). Similar to the margin-wide analysis, seep depth-distribution displayed non-normality in each of the respective regions, as highlighted by the shape of the violin plots (i.e., multimodal data distribution), illustrating scatter rather than concentrated around the median (Figure 3). This nonuniform distribution is consistent with previous observations (Johnson et al., 2015; Riedel et al., 2018).

3.2 Cluster analysis

Testing for patterns in spatial distribution margin-wide revealed that seeps exhibit spatial clustering, as opposed to random or dispersed distributions. Along the margin seven distinct clusters (i.e., hot spots) of high-density seeps were identified (Figure 3). All of the major clusters, except the cluster at Heceta Bank, are in areas where the OAH and landward limit of the GHZS coincide (Figure 3), as discussed in more detail below. In region 1, a single cluster was identified from 200 to 900 m depth at the head of Nitinat Canyon. At this site the OAH and the landward limit of the GHSZ converge (Figure 3 and Supplementary Figure S4), in contrast to the majority of region 1 where the landward limit of the GHSZ has a seaward offset relative to the OAH (Supplementary Figure S3). Region 2 exhibited the highest incidence of clusters, where each of the three clusters occurred at the heads of major submarine canyons, Quinalt and Quillayute, Grays, and Astoria Canyons, that incise the shelf at 200 m. However, seeps in Astoria Canyon extend into the canyon and occur at a range of depths along the canyon thalweg. In contrast to regions 1 and 2, region 3 is devoid of canyons and clusters in this region occur on local structural highs, at Cascade Bench and Heceta Bank. In addition, the highest probability (i.e., peak in kernel density estimation curve) of seeps occurring within the depth range of the landward limit GHSZ is only valid in region 3, as discussed in detail below. A cluster at Coquille Bank was identified in region 4 where the OAH and landward limit of the GHSZ converge. Notably, this cluster is located where an inferred backstop boundary fault (Watt and Brothers, 2020) intersects a unique seafloor seep characterized by gas bubbles containing mantle-derived helium suspected to be sourced from the subducting Gorda plate (Baumberger et al., 2018). In comparison, no cluster was detected directly offshore Coos Bay, despite convergence of the

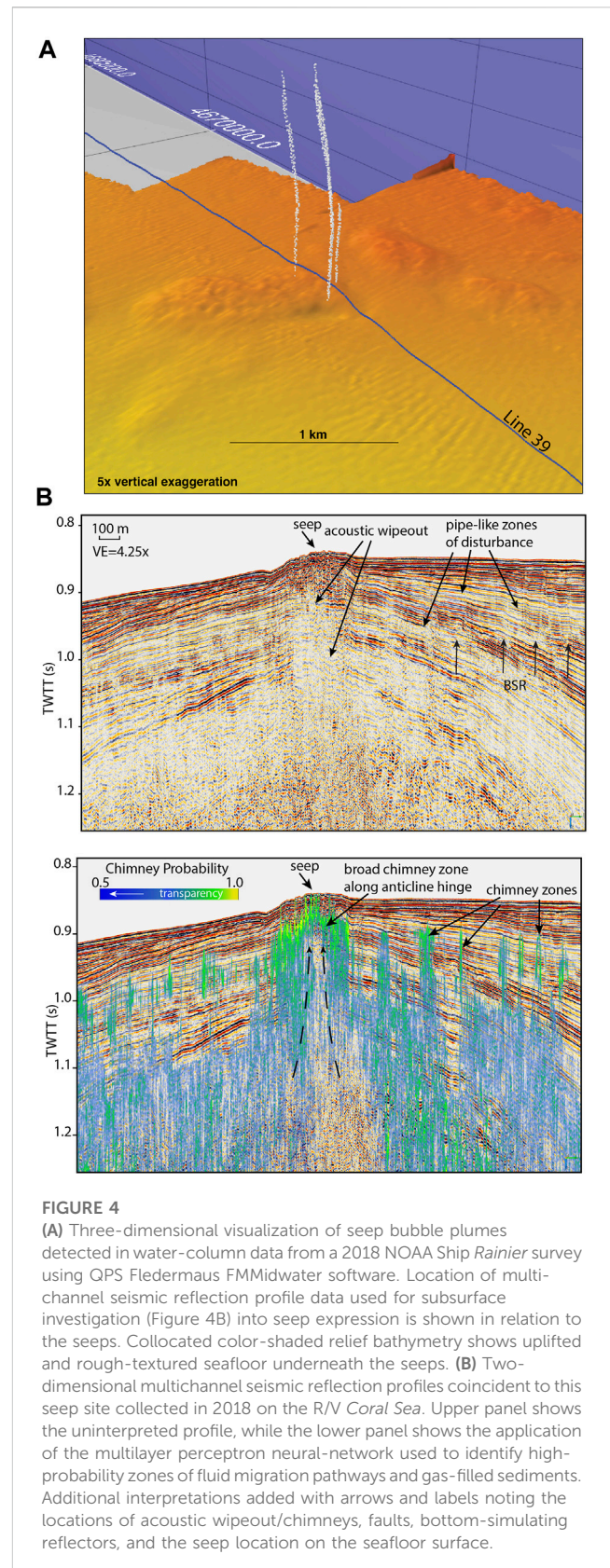


FIGURE 4 (A) Three-dimensional visualization of seep bubble plumes detected in water-column data from a 2018 NOAA Ship *Rainier* survey using QPS Fledermaus FMMidwater software. Location of multi-channel seismic reflection profile data used for subsurface investigation (Figure 4B) into seep expression is shown in relation to the seeps. Collocated color-shaded relief bathymetry shows uplifted and rough-textured seafloor underneath the seeps. (B) Two-dimensional multichannel seismic reflection profiles coincident to this seep site collected in 2018 on the R/V *Coral Sea*. Upper panel shows the uninterpreted profile, while the lower panel shows the application of the multilayer perceptron neural-network used to identify high-probability zones of fluid migration pathways and gas-filled sediments. Additional interpretations added with arrows and labels noting the locations of acoustic wipeout/chimneys, faults, bottom-simulating reflectors, and the seep location on the seafloor surface.

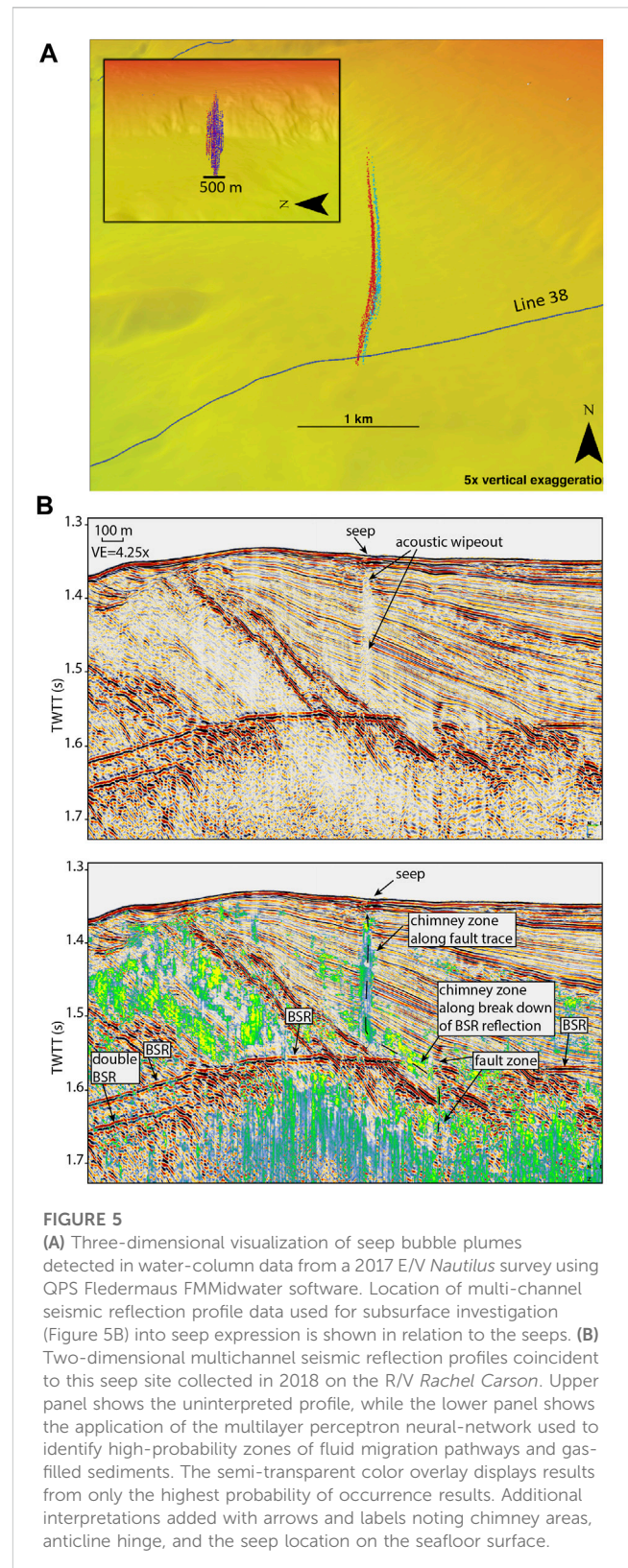
seaward to a depth range of 800 to 2,000 m, where seeps appear to be strongly associated with the OAH rather than the landward limit of the GHSZ (Figure 3). A second cluster was identified around the head of Eel Canyon at the southern terminus of the Cascadia margin and is also where the OAH rejoins with the landward limit of GHSZ.

3.3 Seep site geomorphology in southern Cascadia

The seep depth distribution in southern Cascadia is unique, as captured in the violin plot of region 4 (Figure 3), where most seeps (62%) occur within the GHSZ (>500 m deep), and in an area where there is a distinct seaward divergence of the OAH into deeper water (Supplementary Figure S3). Given the lack of overlap between the OAH and landward limit of the GHSZ in southern Cascadia, the deeper distribution of seeps was investigated in the context of site specific geologic-geomorphic controls. Seeps could have associations with multiple geologic-geomorphic attributes and were therefore assigned up to two primary attributes (Supplementary Table S2). Of the seven types of geologic-geomorphic attributes evaluated for facilitating fluid flow, more than half (52%) of the 278 seep emission sites in southern Cascadia occur on anticlines, with the majority of anticlines located within or seaward of the OAH (Figure 3). In comparison, 16% of seeps were associated with canyons, 14% with the shelfbreak, 11% with seafloor failure scarps, 7% in channels or gullies, and 7% at sites of bedding outcrop. While assigning site specific geologic attributes to all seeps on the Cascadia margin is outside the current scope of the study, we did find that 44% of the seep emission sites in region 3 were located on anticlines, suggesting the strong association of seeps on anticlines carries to morpho-tectonic regions other than region 4.

3.4 Fluid-flow pathways

To further investigate the link between the occurrence of seafloor seepage and underlying geologic structure in southern Cascadia, we combined high-resolution bathymetry, water-column, and two-dimensional MCS data at two seep flare sites in region 4 as representative examples of detection of gas reservoirs and fluid migration pathways. The first example is based on water-column data from 2018 NOAA Ship *Rainier* MBES survey, where three seep flares were detected at ~638 m depth, with fluid emissions reaching a height of 260 m above the seafloor (Figure 4A). Bathymetry and rough seafloor character underneath the seep cluster and the high-intensity backscatter values accompanying these patches suggests the rough seafloor consists of authigenic carbonate precipitation. The seafloor morphology is mostly likely controlled by a broad anticlinal structure, as depicted in the MCS data (line 39 from the R/V *Coral Sea*). Within the anticline and beneath the active seep there is a zone of chaotic reflections and acoustic wipe-out located below the hinge line (Figure 4B). Chimney analysis reveals a broad high-probability zone below the seep field, indicating probable fluid-pathways (Figure 4B). Additional pipe-like zones of disturbance on both sides of the seep field are also



highlighted as high-probability chimney zones. Fluids appear to be focused toward the hinge line where vertical pipes or faults provide a pathway to the seafloor, resulting in seafloor emissions.

The second example is from a seep site identified from water-column data derived from a 2017 E/V *Nautilus* MBES survey at a

water depth of ~995 m depth and flare rising 430 m into the water column. By rotating the 3D perspective from north-south orientation to east-west, a long, thin “bubble curtain” with a horizontal extent of 500 m across is revealed (Figure 5A). Bathymetric shaded relief reveals uplifted and rough seafloor character underneath seep cluster. As depicted in the MCS data (line 38 from the R/V *Rachel Carson*), this seep site is above a normal fault on the flank of a broad anticlinal structure (Figure 5B). As described above, chimney analysis indicates the presence of probable fluid-pathways beneath a hydrate cap (BSR) and likely updip fluid migration through a chimney zone to the seafloor (Figure 5B). The seismic profile shows that at depth, disruption of the BSR coincides with the location of a deeper fault, as well as the presence of a relic (“double”) BSR.

3.5 Authigenic carbonates

Authigenic carbonate $\delta^{13}\text{C}$ values range from -56.73‰ to 10.03‰ with an average value of $-25.21\text{‰} \pm 15.39\text{‰}$ ($n=324$), whereas $\delta^{18}\text{O}$ values range from -1.85‰ – 9.15‰ with an average value of $-3.70\text{‰} \pm 1.67\text{‰}$ ($n=324$) (Supplementary Table S3). Aragonite is the dominant carbonate phase of the authigenic carbonates and is the major component in 57% of the samples, with low and high-Mg calcite accounting for 29% and dolomite present at 13%. There is a $\delta^{13}\text{C}$ range of over 60‰ from samples collected along the margin, and $\delta^{13}\text{C}$ values correlate with both depth and latitude, with statistically significant ($p<0.01$) Pearson-Product Correlation Coefficient ($p<0.01$) of -0.49 and -0.48 , respectively. In contrast, no correlation was found between authigenic carbonate $\delta^{18}\text{O}$ values with either depth or latitude. Based on the aragonite-temperature equation of Grossman and Ku (1986) and seawater $\delta^{18}\text{O}$ value of 0.08‰ SMOW (Bohrmann et al., 1998), the average $\delta^{18}\text{O}$ -derived temperature is $5.0^\circ\text{C} \pm 3.7^\circ\text{C}$, overlapping with CTD bottom water temperatures at a depth range between 150 and 1,600 m (Baker and Prouty, 2022; Prouty and Baker, 2022).

4 Discussion

4.1 Margin-wide seep depth distribution and cluster analysis

The identification of new seep sites in central and southern Cascadia in this study extends our understanding of seep depth distribution along a subducting margin. The margin-wide depth distribution presented here is consistent with other findings that seep density peaks around 500-m depth (Merle et al., 2021), but the non-normality contradicts the assumption of symmetrical probability distribution around ~500 m. Instead of exhibiting symmetrical probability distribution around ~500 m, the margin-wide depth distribution is left-skewed with a long-tail highlighting numerous observations of deep seeps up to 3,100 m. On a regional basis, the probability of seeps occurring within the depth range of the landward limit GHSZ is only valid in region 3 (Figure 3). While the seep distribution is non-random, the clustering described above is not restricted to the 500-m isobath but rather at distinct clusters with

unique geologic and geomorphic characteristics. Whereas Merle et al. (2021) normalized seeps to percent area mapped for only a subset of eight multibeam surveys, we normalized seep occurrence to area mapped using all the co-located footprints from 30 multibeam surveys. Between 200–1,500 m depth, MBES mapping coverage was consistently high (80%–95%), such that our results and interpretation were not significantly hindered by data gaps in survey coverage at different depth bins. Increasing multibeam data acquisition in the 0–200 m water depth range would further refine our estimation of seep density in shallow waters along the margin. The opportunistic discovery of seeps and seep-indicators (i.e., chemosynthetic biota) using ROVs at sites where MBES did not detect seeps is a reminder that, in addition to the temporal ephemerality of seeps releasing detectable gas bubbles, an absence of seeps recorded in MBES surveyed area does not indicate a true absence of seeps.

In regions 1 and 2, the majority of seeps are on the shallow continental shelf (<200 m), with the seep clusters at the heads of canyons in northern Cascadia (Figure 3). Given that the canyons incise the shelf at (or less than) 200 m, it is not surprising that seeps in regions 1 and 2 have the highest probability of occurring at depths less than 200, consistent with previous observations (Johnson et al., 2019). Seep clusters are located at the heads of major submarine canyons except in Astoria Canyon, where seeps span a depth range from 109 to 300 m at the canyon head to 480–1,026 m in the canyon. As suggested by Merle et al. (2021), the large seep distribution in Astoria is likely linked to a combination of factors, with Astoria Canyon deeply incising into the shelf, resulting in steep canyon walls, facilitating massive sidewall and channel levee failures and exposing bedding planes on the mid to lower slope (Hill et al., 2022), thus promoting seepage pathways within the permeable sediment layers. In addition to a high occurrence of seep clusters in canyons in region 2, this region is also characterized by landward migration of the OAH, most likely in response to active extensional faulting. As a result, the OAH overlaps with the landward limit of the GHSZ (Figure 3), which most likely further facilitates focused fluid in these clusters.

Seep depth distribution in the south is progressively deeper but also signifies the only region (region 3) devoid of canyons and where the probability of seeps occurring within the depth range of the landward limit GHSZ is valid (Figure 3). The predominant cluster in region 3 is at Cascade Bench, a topographic high situated between Cascade Head and Tillamook Bay at depth of 400–600 m and inferred to be a paleo-shelf edge formed during the Pleistocene lowstand (McNeill et al., 2000). A second cluster was identified at Heceta Bank, a structural high along the outer shelf caused by subducting seamounts (Tréhu et al., 2012). Within this region, the OAH is co-located with the landward limit of the GHSZ except at Heceta Bank, suggesting some discrepancy of cluster behavior on structural highs with regards to convergence of the OAH and landward limit of the GHSZ.

The overlap between the OAH and the landward limit of the GHSZ may help explain the occurrence of the two clusters in region 4, one at Rogue Canyon and Coquille Bank, a north-south trending double plunging, asymmetrical anticline (Kulm and Bales, 1969), and the other around the head of Eel Canyon. Both sites are places where the OAH and landward limit of the GHSZ converge, along with the presence of submarine canyon heads (the importance of

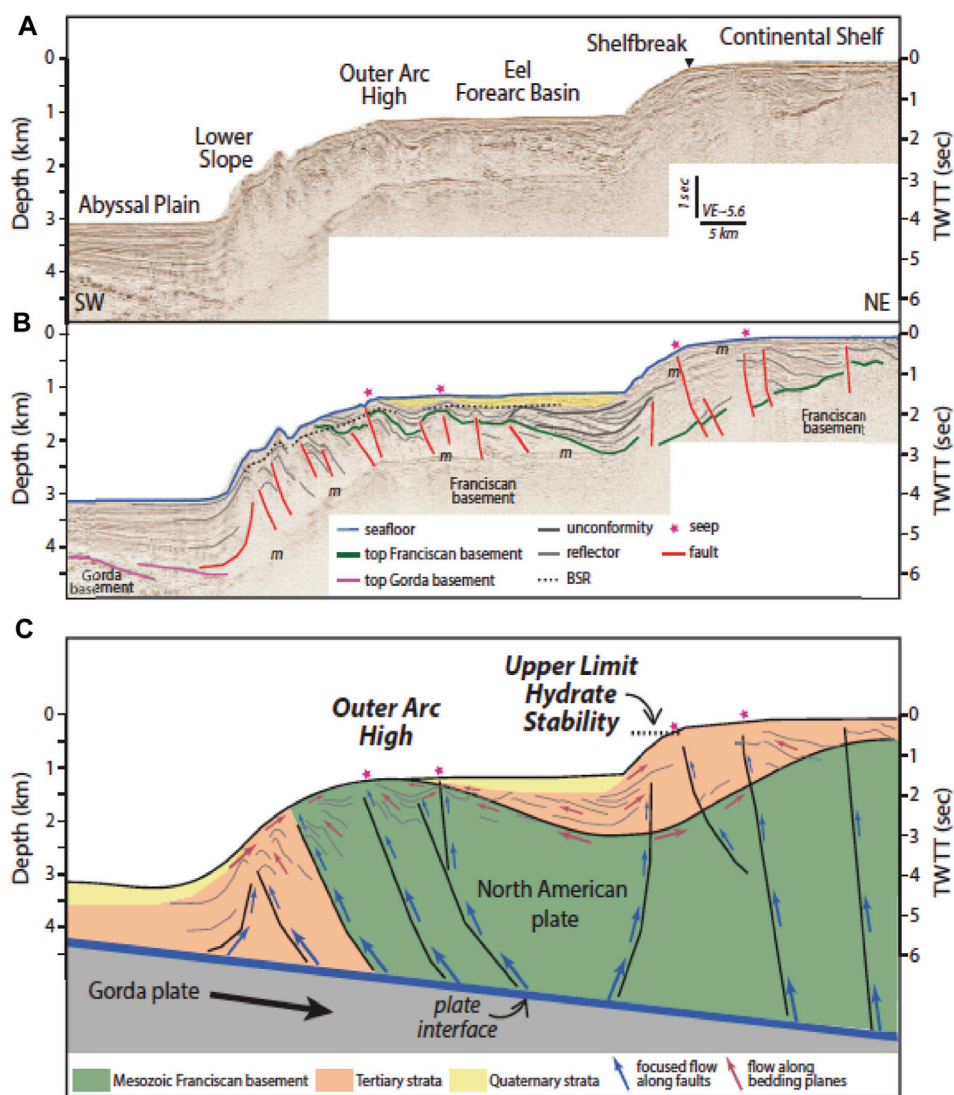


FIGURE 6

Cross-sections of the southern Cascadia margin in Region 4 (location shown in Figure 3), showing the subsurface structure of the outer arc high (OAH) in (A) uninterpreted, (B) interpreted migrated industry seismic profile, Line W675NC-524 (Triezenberg et al., 2016). The OAH in this region forms a broad structural high (10s of km wide) comprised of numerous imbricated thrust faults and associated folds. The OAH bounds the seaward edge of the forearc basin. The seafloor multiple is indicated by "m". (C) shows a conceptual model depicting the OAH as a first-order anticlinal trap that focuses fluid flow along individual faults and bedding planes. Note that within this region the outer arc high and upper limit of hydrate stability are spatially distinct features that each play an important role in focusing fluid seepage at the seafloor. Depth of Franciscan basement is estimated based on nearby interpretations from Gulick et al. (2002).

which was discussed above). Seafloor fluid emission at Coquille Bank may also be further facilitated by a backstop fault formed from the subducting Gorda Plate (Watt and Brothers, 2020) with access to mantle-derived fluids (Baumberger et al., 2018), and associated with a mafic ridge buried beneath the sediments of the accretionary complex from about 43° to 45°N (Fleming and Tréhu, 1999). In the rest of region 4, the OAH and the landward limit of the GHSZ are separated from each other by an average of 23 ± 6.1 km as the OAH deviates seaward around the Eel River Basin. As noted in this study, many seeps occurred in the deep water in association with the OAH, and prolific seep activity was also observed proximal to the channel heads of Trinidad Canyon where a north-south trending fault cuts across the channel heads and the shelfbreak (Balster-Gee et al.,

2023a), but there was a dearth of seeps in the basin between. We posit that the lack of seeps here may be due to high sedimentation rates in the Eel River Basin that cause deposition of mud and silt to drape over the Basin and Trinidad Canyon (Nittrouer, 1999; Sommerfield and Nittrouer, 1999), which may limit sufficient porefluid methane saturation. Whereas gas hydrates tend to concentrate in coarser-grained sandy/silty turbidite sediments (Torres et al., 2008), high sedimentation rate of fine-grained sediment may preclude sufficient porefluid methane saturation. This scenario is consistent with observations by Tréhu and Phrampus (2022) to explain the absence of BSR and extension of the seaward edge of the Eel River Basin well to the west of the theoretical landward edge of the GHSZ. Therefore, we suggest that

the lack of overlap between the OAH and the landward limit of the GHSZ and sedimentation history precludes development of seep cluster anywhere else in region 4.

The discussion above provides an interpretive framework for understanding and potentially predicting seep clusters along a subducting margin and helps address the unresolved origin of seeps at 500 m by identifying processes and characteristics that facilitate focused fluid independently of gas hydrate dissociation in response to contemporary ocean warming. While canyons and structural highs are critical geomorphic features facilitating seep occurrence, overlap between the OAH and the landward limit of the GHSZ may be required for statistically significant clustering of seep emissions. In Cascadia, there is co-occurrence of the OAH (and shelf break) with the downdip end of seismic ruptures and interseismic coupling (McNeill et al., 2000; Booth-Rea et al., 2008; Malatesta et al., 2021). Therefore, there may be links between seep distribution and seismogenic patterns given the release and drainage of fluids from clay dehydration in the transition between locked and seismogenic zone (Saffer and Tobin, 2011). Low permeability and porosity of marine sediment could lead to significant overpressure in these environments and trapping of fluids (Sahling et al., 2008; Saffer and Tobin, 2011). In other words, there is upward/updip fluid migration from zones of peak dehydration and/or elevated pore pressure toward that OAH along permeable stratigraphic layers and fault conduits. The OAH acts as a first-order anticlinal trap that focuses fluid flow along individual faults and bedding plane (Figure 6), as supported by sub-surface data showing where widespread folds channel fluids and gases toward the anticlinal crests, as seen in the structurally controlled seeps offshore Costa Rica (Kluesner et al., 2013). This may not apply to seeps away from the deformation front since dehydration may occur at a shallow depth and near the deformation front (Hyndman and Wang, 1993; Hyndman, 2007), given the high temperatures of the very young hot subducting plate (e.g., Hyndman, 2007). In contrast, near Hydrate Ridge, Torres et al. (2004) and Teichert et al. (2005) found an increase in deep freshening eastward (i.e., relative to the toe), whereas accretion at the westernmost sites is too recent for the sediments to have undergone significant illitization. While differentiating fluids from dehydration relative to hydrate dissociation requires analysis of porefluids, the co-location of the seep clusters with the OAH and inferred downdip end of interseismic coupling in Cascadia is intriguing and warrants further investigation.

4.2 Fluid source

As a proxy for the composition of fluids, the authigenic carbonate isotope values suggest a range of sources, including thermogenic decomposition of organic matter and biogenic mediation from microbial activity (Claypool et al., 1985). The average authigenic carbonate $\delta^{13}\text{C}$ values ($-53.53\text{‰} \pm 1.95\text{‰}$) at the Astoria deep sites (>800 m) are depleted relative to carbonate $\delta^{13}\text{C}$ values at the shallow site (500 m; $-28.51\text{‰} \pm 2.26\text{‰}$), yielding a difference of 25‰, similar in magnitude between gas samples at the shallow versus deeper Astoria sites (Baumberger et al., 2018). As described in Baumberger et al. (2018), anaerobic oxidation of methane (AOM), as well as incorporation of dissolved inorganic

carbon (DIC) and co-existing CO_2 and its associated shift in isotope composition, can produce heavy $\delta^{13}\text{C}$ values that mimic a thermogenic origin (Pohlman et al., 2009). Given gas isotopic and hydrocarbon composition indicative microbial methane at Astoria (Baumberger et al., 2018), the heavier carbonate $\delta^{13}\text{C}$ values at the shallow site are in line with ^{13}C -enrichment by AOM.

In contrast, at Coquille the presence of only thermogenic methane (Collier and Lilley, 2005; Baumberger et al., 2018) provides an opportunity to calibrate the range in carbonate $\delta^{13}\text{C}$ values (-26.50 to -17.76‰) in the absence of mixing with microbial sources. Taken together, data from Coquille and Astoria can be used as endmember values for estimating contribution from microbial and thermogenic methane sources to carbonate $\delta^{13}\text{C}$ values at other sites where both sources are identified, such as at Heceta Bank (Baumberger et al. (2018)). For example, carbonate $\delta^{13}\text{C}$ values greater than the range reported at Coquille can be explained by oxidation of methane and DIC incorporation, whereas carbonate $\delta^{13}\text{C}$ values less than this range reflect mixing with microbial methane. Assuming endmember microbial and thermogenic $\delta^{13}\text{C}$ values from Baumberger et al. (2018), mixing with a microbial methane at Heceta Bank could contribute to a depletion of 15‰, equivalent to a contribution of less than 10% from microbial methane.

The inverse correlation between $\delta^{13}\text{C}$ values and depth supports earlier views that seeps from within the gas hydrate stability zone are of microbial origin and seeps from the upper slope and the shelf have a thermogenic source (e.g., Collier and Lilley, 2005; Heeschen et al., 2005; Baumberger et al., 2018). However, the discussion above also demonstrates how processes impacting fluid chemistry, such as mixing and AOM, can impact the fluid isotopic composition (Pohlman et al., 2009) and ultimately alter the archived fluid-source signature in the authigenic carbonates. In addition, gas hydrate dissociation can provide a potential source of ^{18}O -enriched fluids, which releases hydrate water and contributes to enrichment by up to 3.5‰ (Maekawa, 2004). Samples with ^{18}O -enriched carbonate values yield unrealistically cold temperatures ($<2^\circ\text{C}$) relative to CTD bottom water data (Baker and Prouty, 2022; Prouty and Baker, 2022), indicating influence from ^{18}O -enriched fluid source. Margin-wide carbonate $\delta^{18}\text{O}$ values and mineralogy, however, support shallow precipitation of aragonite driven by AOM and in isotopic equilibrium with seawater.

4.3 Anticlines as trappings for focused fluid flow

While the occurrence of seep clusters and the justification for their distribution may help explain the spatial distribution of seeps along the Cascadia margin, it does not explain the range or probability of seep depth distribution across the four regions. Instead, the site-specific investigation of region 4 reveals quantitative links between seafloor geomorphology/geology and seep occurrence. As reported above, over half of the seeps in region 4 occur on anticlines. This characteristic of region 4 helps to explain the probability depth distribution of seeps within the GHSZ. As shown in Figure 3 the OAH diverges seaward, representing a unique feature of southern Cascadia not observed elsewhere along the margin. According to Tréhu and Phrampus

(2022), this region is also marked by the greatest distance between the landward-most BSR pick and 500 m contour (Supplementary Figure S4). Given that the OAH is an actively deforming portion of the margin, younger anticlines are formed from west to east (i.e., seaward or within the OAH) by uplift and horizontal compression as the deformation front steps seaward (Carson et al., 1974; McNeill et al., 1999; McCrory et al., 2002). In this region, the BSR is also tens of km seaward of the landward limit of the GHSZ where accretion of trench sediments forms a thick accretionary wedge (Tréhu and Phrampus, 2022). This spatial pattern highlights the potential role of the OAH on not only seep distribution but hydrate formation, where accretionary wedge tectonics and seafloor morphology serve as structural controls on fluid reservoirs, trapping, and transport. The 2-D conceptual model shown in Figure 6 demonstrates fluid flow paths and seafloor seepage features that are dependent on folds and fault patterns. Whereas convergence rates are similar along the Cascadia margin, the structural style and width of the actively deforming outer wedge varies along-strike, with a narrower wedge in the south relative to wider wedge in the north (Watt and Brothers, 2020). As a result, the narrower wedge forms a steeper accretionary prism with closely spaced faults/anticlines that stack on top of one another (i.e., imbricate faulting). In contrast, the wide wedge in northern Cascadia forms widely spaced anticlines. Region 3 is also characterized by a relatively high occurrence of seeps on anticlines characterized by mixed or dual vergence (Watt and Brothers, 2020), resulting in more-symmetrical fold structures and steeper seafloor gradients along the fold limbs evident in seismic data (Booth-Rea et al., 2008; Phrampus et al., 2017).

The occurrence of seeps on anticlines follows the conceptual models of focused fluid flow and gas migration along the crest of an anticline described by Paull et al. (2008), such as observed offshore north Panama (Reed et al., 1990), Costa Rica (Kluesner et al., 2013), and along the Queen Charlotte Fault (Prouty et al., 2020), where folding, thrust faulting, and sedimentation along a deformation front may facilitate fluid flow and seafloor venting. This relationship has been previously noted on the Cascadia margin, where the development of anticlinal ridges controls the location of seepage and are strongly correlated with vertical fluid migration paths (Carson et al., 1991; Carson et al., 1994; Johnson et al., 2003). Similarly, Tréhu et al. (1999) speculated positive feedback between gas hydrate formation and anticlines. Merle et al. (2021) also noted that deeper seeps (>525 m) were coincident with major compressional anticlinal (and diapiric ridges) within the accretionary prism. The efficiency of anticlines to trap and focus fluid flow is clearly seen in the MSC data and chimney analysis (Figures 4, 5), where broad high-probability zones of fluid migration and areas of chaotic reflections and acoustic wipe-out are located below the anticline hinge line. At depth, disruption of the BSR coincides with the location of a deeper fault, which is likely channeling fluids and causing breakdown of the hydrate cap. Upon intersecting the first fault up-dip, the gas/fluid presumably migrates upward along a path of least resistance to the seafloor. The seismic profile also shows the presence of a relic ("double") BSR (Figure 5), possibly caused by episodes of uplift leading to shoaling/reestablishment of the BSR due to changing thermal conditions. This analysis also illustrates how faults disrupt the BSR (and presumably hydrate stability) and provide a pathway

for fluids and gas to reach the seafloor, resulting in seafloor emissions. Hydraulic fracturing can also serve as a gas conduit. For example, along the southern Hikurangi margin in Aotearoa/New Zealand, anticlines act as a focusing mechanism for the fluids, where there is sufficient upward pressure to overcome the lithostatic load of the overburden and blow-out, or fracture, leading to a vertical pathway to the seafloor (Crutchley et al., 2021).

4.4 Tectonic framework for seep distribution

Taken together, this quantitative approach has identified characteristics/features as well as processes along the margin that facilitate seep emissions that operate independently of gas hydrate dissociation in response to contemporary ocean warming. In doing so, this study provides an expanded interpretive framework for understanding the controls and influencing factors on the depth and spatial distribution of seeps along the Cascadia margin and is consistent with stable gas hydrate occurrences even under future scenarios of warming bottom waters (Ruppel, 2011; Ruppel and Kessler, 2017). This interpretive framework may also be applied to other subduction margins that are dominated by accretion, such as the southern Hikurangi margin offshore Aotearoa/New Zealand (Barnes et al., 2010), where high fluid pressures play an important role in maintaining thrust wedges (Saffer and Bekins, 2002). For example, the majority of seeps on the southern Hikurangi margin were detected on crests of thrust-faulted anticlinal ridges at 700–1,200 m and where a network of near-surface faults and chimneys facilitates fluid expulsion and a breakdown in BSR (Mountjoy et al., 2009a; Barnes et al., 2010; Law et al., 2010; Crutchley et al., 2018; Watson et al., 2020). While seeps along the Hikurangi margin are consistently located above the deforming backstop, seep distribution based on MBES water column backscatter data is not uniform, and similar to the Cascadia margin, no evidence was found to suggest clustering of seeps near the landward limit of the GHSZ (650 m; Supplementary Figure S5). Instead, seeps in the north are concentrated near the shelf break within the Tuaheni Landslide Complex, where a combination of factors have contributed to slope instability, including earthquake ground shaking and gas release (Mountjoy et al., 2009b; Mountjoy et al., 2014; Gross et al., 2018; Carey et al., 2022; Crutchley et al., 2022). In comparison, seeps in the south occupy deeper water depths and are found to cluster along the crests of parallel ridges (Supplementary Figure S6), where gas is trapped beneath large sedimentary folds/anticlines formed by deep-seated thrust faults, and focused fluid flow is facilitated by both faults and hydraulic fractures (Crutchley et al., 2021).

This comparison highlights the role of regional geologic structures influencing clusters of focused fluid flow, as well as detailing margin-wide variability in seep distribution along both margins. For example, the largest depth range of seeps is located in the relatively narrow southern end of both margins where there is a transition from subduction to strike-slip deformation (Barnes et al., 2010; Watt and Brothers, 2020). At this transition, strike-slip faults that trend across the slope (Gulick et al., 2002) may provide additional near-vertical pathways for fluid flow across a range of water depths. The importance of the geometry of geologic structures to influence spatial location and character of seeps has been

previously documented (Kulm et al., 1986; Le Pichon et al., 1992). However, results from our study, which demonstrate the importance of both geometry of geologic structures and the role of the margin-wide morphotectonics, may expand previous models of the distribution of fluid expulsion along subduction zones.

5 Conclusion

By applying a spatial and statistical analysis to an expanded seep database, coupled with multibeam bathymetry and chimney meta-attribute analysis of seismic reflection profiles, we show that gas hydrate stability is one of many other controls, primarily morphologic and tectonic, on seep distribution in Cascadia. Seep distribution along the margin is non-random, but instead of clustering along the 500-m isobath, seep clusters are dominated by the presence of canyons and topographical highs. New findings from this study suggest that co-location of the outer arc high (OAH) and landward limit of the gas hydrate stability zone (GHSZ) may be a prerequisite for seep cluster development in Cascadia, where a broad area of deformation overlaps a zone where hydrates are particularly vulnerable to dissociation, such as in areas with focused uplift and in headward-eroding canyons. The wide range in seep depth distribution, and in particular the trend toward deeper depths in southern Cascadia can also be linked to the location of the OAH where the development of thrust-faulted anticlines along the seaward edge of the Eel River forearc basin plays a crucial role in facilitating focused fluid flow and seep emissions despite being within the GHSZ. Refining models of fluid expulsion is critical, given the importance of fluid flow on plate boundary seismogenesis, global carbon budgets, and supporting sensitive seafloor ecosystems.

Data availability statement

The datasets presented in this study can be found in online repositories. The names of the repository/repositories and accession number(s) can be found in the article/[Supplementary Material](#).

Author contributions

JR compiled and prepared datasets used, performed all spatial and statistical analyses, created publication figures and tables, and assisted with manuscript preparation. NP conceived the study, analyzed carbonate geochemistry, and wrote the paper with input from all authors. JC identified seep locations from MBES water column data and helped determine geologic attributes of seep areas. JWK helped collect and process the MCS data, conducted the neural-network chimney analysis, and provided interpretation of the results. JW and JCH provided input on the tectonic setting and regional geology. JW also helped determine geological attributes of

seep sites in region 4. SW and JIH contributed seeps database for the Hikurangi margin and assisted with manuscript preparation, focusing on the comparison to the Hikurangi margin. NM helped collect and process the MCS data. All authors contributed to the article and approved the submitted version.

Funding

The U.S. Geological Survey Coastal and Marine Geohazards Resource Program funded this study with additional support from the USGS Environments Program through the Outer Continental Shelf study and Bureau of Ocean and Energy Management (BOEM) Interagency Agreement.

Acknowledgments

We thank C. Ruppel (USGS), D. Brothers (USGS), P. Dartnell (USGS) and J. Beeson (NOAA) for helpful discussions, C. Paull and L. Lemon (Monterey Bay Aquarium Research Institute) for sharing ROV video annotation logs of chemosynthetic biota, T. Baumberger (Oregon State University) and S. Merle (Oregon State University) for sharing archived authigenic carbonate samples, and S. Pit (UCSC), S. Stremmler (UCSC), C. Carney, and A. Gartman (USGS) for sample preparation and geochemical analysis. Input from reviewers improved the manuscript. Any use of trade, firm, or product names is for descriptive purposes only and does not imply endorsement by the U.S. Government.

Conflict of interest

The authors declare that the research was conducted in the absence of any commercial or financial relationships that could be construed as a potential conflict of interest.

Publisher's note

All claims expressed in this article are solely those of the authors and do not necessarily represent those of their affiliated organizations, or those of the publisher, the editors and the reviewers. Any product that may be evaluated in this article, or claim that may be made by its manufacturer, is not guaranteed or endorsed by the publisher.

Supplementary material

The Supplementary Material for this article can be found online at: <https://www.frontiersin.org/articles/10.3389/feart.2023.1205211/full#supplementary-material>

References

- Audet, P., Bostock, M. G., Mercier, J. P., and Cassidy, J. F. (2008). Morphology of the Explorer–Juan de Fuca slab edge in northern Cascadia: Imaging plate capture at a ridge-trench-transform triple junction. *Geology* 36, 895–898. doi:10.1130/g25356a.1
- Baker, M. C., and Prouty, N. G. (2022). *Conductivity temperature depth data collected october–november 2019 offshore of California and Oregon*. U.S. Geological Survey Data Release. doi:10.5066/P9F7K9F2
- Balster-Gee, A. F., Kluesner, J. W., Watt, J. T., Hill, J. C., Brothers, D. S., Michalak, M. J., et al. (2023a). *Multichannel sparker and chirp seismic reflection data collected during USGS field activity 2018–658-FA between cape blanco and cape Mendocino in october of 2018*. U.S. Geological Survey data release. doi:10.5066/P9MYL7WJ
- Balster-Gee, A. F., Miller, N. C., Watt, J. T., Roland, E., Kluesner, J. K., Heller, S. J., et al. (2023b). *High-resolution multichannel sparker seismic-reflection and chirp subbottom data acquired along the Cascadia margin during USGS field activity 2019-024-FA*. U.S. Geological Survey Data Release. doi:10.5066/P96ZBXK8
- Barnard, W. D. (1973). *Late Cenozoic sedimentation on the Washington continental slope*. University of Washington.
- Barnes, P. M., Lamarche, G., Bialas, J., Henrys, S., Pecher, I., Netzeband, G. L., et al. (2010). Tectonic and geological framework for gas hydrates and cold seeps on the Hikurangi subduction margin, New Zealand. *Mar. Geol.* 272, 26–48. doi:10.1016/j.margeo.2009.03.012
- Baumberger, T., Embley, R. W., Merle, S. G., Lilley, M. D., Raineault, N. A., and Lupton, J. E. (2018). Mantle-derived helium and multiple methane sources in gas bubbles of cold seeps along the Cascadia continental margin. *Geochem. Geophys. Geosystems* 19, 4476–4486. doi:10.1029/2018GC007859
- Berndt, C., Feseker, T., Treude, T., Krastel, S., Liebetrau, V., Niemann, H., et al. (2014). Temporal constraints on hydrate-controlled methane seepage off Svalbard. *Science* 343, 284–287. doi:10.1126/science.1246298
- Bohrmann, G., Greinert, J., Suess, E., and Torres, M. (1998). Authigenic carbonates from the Cascadia subduction zone and their relation to gas hydrate stability. *Geology* 26, 647–650. doi:10.1130/0091-7613(1998)026<0647:acftcs>2.3.co;2
- Booth-Rea, G., Klaeschen, D., Grevemeyer, I., and Reston, T. (2008). Heterogeneous deformation in the Cascadia convergent margin and its relation to thermal gradient (Washington, NW USA). *Tectonics* 27. doi:10.1029/2007TC002209
- Brothers, D. S., Ruppel, C., Kluesner, J. W., Ten Brink, U. S., Chaytor, J. D., Hill, J. C., et al. (2014). Seabed fluid expulsion along the upper slope and outer shelf of the U.S. Atlantic continental margin. *Geophys. Res. Lett.* 41, 96–101. doi:10.1002/2013GL058048
- Canfield, D. E., Kristensen, E., and Thamdrup, B. (2005). Aquatic geomicrobiology. *Adv. Mar. Biol.* 48, 1–599. doi:10.1016/s0065-2881(05)48017-7
- Carey, J. M., Mountjoy, J. J., Crutchley, G. J., Petley, D. N., Holden, C. F., Kaneko, Y., et al. (2022). Episodic movement of a submarine landslide complex driven by dynamic loading during earthquakes. *Geomorphology* 408, 108247. doi:10.1016/j.geomorph.2022.108247
- Carson, B., Holmes Mark, L., Umstatter, K., Strasser Jeffrey, C., Johnson, H. P., Tarney, J., et al. (1991). Fluid expulsion from the Cascadia accretionary prism: Evidence from porosity distribution, direct measurements, and GLORIA imagery. *Philosophical Trans. R. Soc. Lond. Ser. A Phys. Eng. Sci.* 335, 331–340. doi:10.1098/rsta.1991.0049
- Carson, B., Seke, E., Paskevich, V., and Holmes, M. L. (1994). Fluid expulsion sites on the Cascadia accretionary prism: Mapping diagenetic deposits with processed GLORIA imagery. *J. Geophys. Res. Solid Earth* 99, 11959–11969. doi:10.1029/94JB00120
- Carson, B., Yuan, J., Myers, P. B., Jr, and Barnard, W. D. (1974). Initial deep-sea sediment deformation at the base of the Washington continental slope: A response to subduction. *Geology* 2, 561–564. doi:10.1130/0091-7613(1974)2<561:idsdat>2.0.co;2
- Clarke, J. S. H., and Carver, G. A. (1992). Late Holocene tectonics and paleoseismicity, southern Cascadia subduction zone. *Science* 255, 188–192. doi:10.1126/science.255.5041.188
- Claypool, G. E., Threlkeld, C. N., Mankiewicz, P. N., Arthur, M. A., and Anderson, T. F. (1985). *Isotopic composition of interstitial fluids and origin of methane in slope sediment of the Middle America Trench, Deep Sea Drilling Project Leg 84. Initial reports DSDP, Leg 84*. Balboa to Manzanillo, 683–691.
- Clift, P., and Vannucchi, P. (2004). Controls on tectonic accretion versus erosion in subduction zones: Implications for the origin and recycling of the continental crust. *Rev. Geophys.* 42. doi:10.1029/2003RG000127
- Cochrane, G. R., and Lewis, B. T. (1984). Comparison of structures in underthrusting and overthrusting lower slope sediments of the Wasington-Oregon convergent margin [abs. *EOS Am. Geophys. Union Trans.* 65, 1089.
- Collett, T. S. (2009). Natural gas hydrates: A review, in natural gas hydrates. Energy resource potential and associated geologic hazards. *AAPG Mem.* 89, 146–219. doi:10.1306/13201101M891602
- Collier, R. W., and Lilley, M. D. (2005). Composition of shelf methane seeps on the Cascadia continental margin. *Geophys. Res. Lett.* 32, L06609. doi:10.1029/2004GL022050
- Connolly, D. L. (2015). Visualization of vertical hydrocarbon migration in seismic data: Case studies from the Dutch North Sea. *Interpretation* 3, SX21–SX27. doi:10.1190/INT-2015-0007.1
- Conrad, J. E., and Rudebusch, J. A. (2023). *Methane seeps derived from water-column acoustic backscatter data collected along Cascadia margin offshore Oregon and Northern California, 2018–2021*. U.S. Geological Survey Data Release. doi:10.5066/P9TW2X7Y
- Crutchley, G. J., Elger, J., Kuhlmann, J., Mountjoy, J. J., Orpin, A., Georgiopolou, A., et al. (2022). Investigating the basal shear zone of the submarine Tuaheni landslide complex, New Zealand: A core-log-seismic integration study. *J. Geophys. Res. Solid Earth* 127. e2021JB021997. doi:10.1029/2021JB021997
- Crutchley, G. J., Kroeger, K. F., Pecher, I. A., and Gorman, A. R. (2018). How tectonic folding influences gas hydrate formation: New Zealand’s Hikurangi subduction margin. *Geology* 47, 39–42. doi:10.1130/G45151.1
- Crutchley, G. J., Mountjoy, J. J., Hillman, J. I. T., Turco, F., Watson, S., Flemings, P. B., et al. (2021). Upward-doming zones of gas hydrate and free gas at the bases of gas chimneys, New Zealand’s Hikurangi margin. *J. Geophys. Res. Solid Earth* 126, e2020JB021489. doi:10.1029/2020JB021489
- DeMets, C., Gordon, R. G., and Argus, D. F. (2010). Geologically current plate motions. *Geophys. J. Int.* 181, 1–80. doi:10.1111/j.1365-246X.2009.04491.x
- Fleming, S. W., and Tréhu, A. M. (1999). Crustal structure beneath the central Oregon convergent margin from potential-field modeling: Evidence for a buried basement ridge in local contact with a seaward dipping backstop. *J. Geophys. Res. Solid Earth* 104, 20431–20447. doi:10.1029/1999jb900159
- Goldfinger, C., Kulm, L. D., Yeats, R. S., Appelgate, B., Mackay, M. E., and Moore, G. F. (1992). Transverse structural trends along the Oregon convergent margin: Implications for Cascadia earthquake potential and crustal rotations. *Geology* 20, 141–144. doi:10.1130/0091-7613(1992)020<0141:tstato>2.3.co;2
- Goldfinger, C., Kulm, L. D., Yeats, R. S., Appelgate, T. B., Jr, Mackay, M. E., and Cochrane, G. R. (1991). *Active strike-slip faulting and folding of the Cascadia plate boundary and forearc in central and northern Oregon*. U.S. Geological Survey Open-File Report. doi:10.3133/ofr914415
- Goldfinger, C., Kulm, L. D., Yeats, R. S., McNeill, L., and Hummon, C. (1997). Oblique strike-slip faulting of the central Cascadia submarine forearc. *J. Geophys. Res. Solid Earth* 102, 8217–8243. doi:10.1029/96jb02655
- Gross, F., Mountjoy, J. J., Crutchley, G. J., Böttner, C., Koch, S., Bialas, J., et al. (2018). Free gas distribution and basal shear zone development in a subaqueous landslide – insight from 3D seismic imaging of the Tuaheni Landslide Complex, New Zealand. *Earth Planet. Sci. Lett.* 502, 231–243. doi:10.1016/j.epsl.2018.09.002
- Grossman, E., and Ku, T. L. (1986). Oxygen and carbon isotope fractionation in biogenic aragonite: Temperature effects. *Isot. Geosci.* 59, 59–74. doi:10.1016/0168-9622(86)90057-6
- Gulick, S. P. S., Meltzer, A. S., and Clarke, S. H., Jr. (2002). Effect of the northward-migrating Mendocino triple junction on the Eel River forearc basin, California: Stratigraphic development. *GSA Bull.* 114, 178–191. doi:10.1130/0016-7606(2002)114<0178:EOTNMM>2.0.CO;2
- Han, S., Bangs, N. L., Carbotte, S. M., Saffer, D. M., and Gibson, J. C. (2017). Links between sediment consolidation and Cascadia megathrust slip behaviour. *Nat. Geosci.* 10, 954–959. doi:10.1038/s41561-017-0007-2
- Hautala, S. L., Solomon, E. A., Johnson, H. P., Harris, R. N., and Miller, U. K. (2014). Dissociation of Cascadia margin gas hydrates in response to contemporary ocean warming. *Geophys. Res. Lett.* 41, 8486–8494. doi:10.1002/2014GL0261606
- Heeschen, K. U., Collier, R. W., De Angelis, M. A., Suess, E., Rehder, G., Linke, P., et al. (2005). Methane sources, distributions, and fluxes from cold vent sites at Hydrate Ridge, Cascadia Margin. *Glob. Biogeochem. Cycles* 19. doi:10.1029/2004GB002266
- Heggland, R. (2005). “Using gas chimneys in seal integrity analysis: A discussion based on case histories,” in *Evaluating Fault and cap rock seals*. Editors P. Boulton and J. Kaldi (American Association of Petroleum Geologists).
- Hein, J. R., Mizell, K., and Barnard, P. L. (2013). Sand sources and transport pathways for the San Francisco Bay coastal system, based on X-ray diffraction mineralogy. *Mar. Geol.* 345, 154–169. doi:10.1016/j.margeo.2013.04.003
- Hill, J. C., Watt, J. T., and Brothers, D. S. (2022). Mass wasting along the Cascadia subduction zone: Implications for abyssal turbidite sources and the earthquake record. *Earth Planet. Sci. Lett.* 597, 117797. doi:10.1016/j.epsl.2022.117797
- Hyndman, R. D. (2007). “2. The seismogenic zone of subduction thrust faults: What we know and don’t know,” in *The seismogenic zone of subduction thrust faults*. Editors H. D. Timothy and M. Casey (New York Chichester, West Sussex: Columbia University Press), 15–40.
- Hyndman, R. D., and Wang, K. (1993). Thermal constraints on the zone of major thrust earthquake failure: The Cascadia Subduction Zone. *J. Geophys. Res. Solid Earth* 98, 2039–2060. doi:10.1029/92JB02279
- Johnson, H. P., Merle, S., Salmi, M., Embley, R., Sampaga, E., and Lee, M. (2019). Anomalous concentration of methane emissions at the continental shelf edge of the northern Cascadia margin. *J. Geophys. Res. Solid Earth* 124, 2829–2843. doi:10.1029/2018JB016453
- Johnson, H. P., Miller, U. K., Salmi, M. S., and Solomon, E. A. (2015). Analysis of bubble plume distributions to evaluate methane hydrate decomposition on the

- continental slope. *Geochem. Geophys. Geosystems* 16, 3825–3839. doi:10.1002/2015GC005955
- Johnson, J. E., Goldfinger, C., and Suess, E. (2003). Geophysical constraints on the surface distribution of authigenic carbonates across the Hydrate Ridge region, Cascadia margin. *Mar. Geol.* 202, 79–120. doi:10.1016/S0025-3227(03)00268-8
- Joung, D., Ruppel, C., Southon, J., Weber, T. S., and Kessler, J. D. (2022). Negligible atmospheric release of methane from decomposing hydrates in mid-latitude oceans. *Nat. Geosci.* 15, 885–891. doi:10.1038/s41561-022-01044-8
- Judd, A., and Hovland, M. (2007). *Seabed fluid flow: The impact on geology, biology and the marine environment*. Cambridge University Press.
- Ketzer, M., Praeg, D., Rodrigues, L. F., Augustin, A., Pivel, M. A. G., Rahmati-Abkenar, M., et al. (2020). Gas hydrate dissociation linked to contemporary ocean warming in the southern hemisphere. *Nat. Commun.* 11, 3788. doi:10.1038/s41467-020-17289-z
- Kluesner, J., Brothers, D., Hart, P., Miller, N., and Hatcher, G. (2019). Practical approaches to maximizing the resolution of sparker seismic reflection data. *Mar. Geophys. Res.* 40, 279–301. doi:10.1007/s11001-018-9367-2
- Kluesner, J. W., and Brothers, D. S. (2016). Seismic attribute detection of faults and fluid pathways within an active strike-slip shear zone: New insights from high-resolution 3D P-Cable™ seismic data along the Hosgri Fault, offshore California. *Interpretation* 4, SB131–SB148. doi:10.1190/INT-2015-0143.1
- Kluesner, J. W., Silver, E. A., Bangs, N. L., McIntosh, K. D., Gibson, J., Orange, D., et al. (2013). High density of structurally controlled, shallow to deep water fluid seep indicators imaged offshore Costa Rica. *Geochem. Geophys. Geosystems* 14, 519–539. doi:10.1002/ggge.20058
- Kulm, L. D., and Bales, W. E. (1969). Shallow structure and sedimentation of upper continental slope off southern and central Oregon: A preliminary investigation. *AAPG Bull.* 53, 472. doi:10.1306/5d25c68f-16c1-11d7-8645000102c1865d
- Kulm, L. D., Suess, E., Moore, J. C., Carson, B., Lewis, B. T., Ritger, S. D., et al. (1986). Oregon subduction zone: Venting, fauna, and carbonates. *Science* 231, 561–566. doi:10.1126/science.231.4738.561
- Law, C. S., Nodder, S. D., Mountjoy, J. J., Marriner, A., Orpin, A., Pilditch, C. A., et al. (2010). Geological, hydrodynamic and biogeochemical variability of a New Zealand deep-water methane cold seep during an integrated three-year time-series study. *Mar. Geol.* 272, 189–208. doi:10.1016/j.margeo.2009.06.018
- Le Pichon, X., Kobayashi, K., and Crew, K.-N. S. (1992). Fluid venting activity within the eastern nankai trough accretionary wedge: A summary of the 1989 kaiko-nankai results. *Earth Planet. Sci. Lett.* 109, 303–318. doi:10.1016/0012-821x(92)90094-c
- Ligtenberg, J. H. (2005). Detection of fluid migration pathways in seismic data: Implications for fault seal analysis. *Basin Res.* 17, 141–153. doi:10.1111/j.1365-2117.2005.00258.x
- Maekawa, T. (2004). Experimental study on isotopic fractionation in water during gas hydrate formation. *Geochem. J.* 38, 129–138. doi:10.2343/geochemj.38.129
- Malatesta, L. C., Bruhat, L., Finnegan, N. J., and Olive, J.-a. L. (2021). Co-Location of the downdip end of seismic coupling and the continental shelf break. *J. Geophys. Res. Solid Earth* 126, e2020JB019589. doi:10.1029/2020JB019589
- McCaffrey, R., Qamar, A. I., King, R. W., Wells, R., Khazaradze, G., Williams, C. A., et al. (2007). Fault locking, block rotation and crustal deformation in the Pacific Northwest. *Geophys. J. Int.* 169, 1315–1340. doi:10.1111/j.1365-246X.2007.03371.x
- Mccrory, P. A., Foster, D. S., Danforth, W. W., and Hamer, M. R. (2002). “Crustal deformation at the leading edge of the Oregon coast range block, offshore Washington (Columbia river to hoh river),” in *Professional paper*. 0 ed. Version 1.
- McNeill, L. C., Goldfinger, C., Kulm, L. D., and Yeats, R. S. (2000). Tectonics of the Neogene Cascadia forearc basin: Investigations of a deformed late Miocene unconformity. *GSA Bull.* 112, 1209–1224. doi:10.1130/0016-7606(2000)112<1209:totnct>2.0.co;2
- McNeill, L. C., Goldfinger, C., Yeats, R. S., and Kulm, L. D. (1999). The effects of upper plate deformation on records of prehistoric Cascadia subduction zone earthquakes. *Geol. Soc. Lond. Spec. Publ.* 146, 321–342. doi:10.1144/gsl.sp.1999.146.01.19
- McNeill, L. C., and Henstock, T. J. (2014). Forearc structure and morphology along the Sumatra-Andaman subduction zone. *Tectonics* 33, 112–134. doi:10.1002/2012TC003264
- Merle, S. G., Embley, R. W., Johnson, H. P., Lau, T.-K., Phrampus, B. J., Raineault, N. A., et al. (2021). Distribution of methane plumes on Cascadia margin and implications for the landward limit of methane hydrate stability. *Front. Earth Sci.* 9. doi:10.3389/feart.2021.531714
- Mountjoy, J. J., Barnes, P. M., and Pettinga, J. R. (2009a). Morphostructure and evolution of submarine canyons across an active margin: Cook Strait sector of the Hikurangi Margin, New Zealand. *Mar. Geol.* 260, 45–68. doi:10.1016/j.margeo.2009.01.006
- Mountjoy, J. J., Mckean, J., Barnes, P. M., and Pettinga, J. R. (2009b). Terrestrial-style slow-moving earthflow kinematics in a submarine landslide complex. *Mar. Geol.* 267, 114–127. doi:10.1016/j.margeo.2009.09.007
- Mountjoy, J. J., Pecher, I., Henrys, S., Crutchley, G., Barnes, P. M., and Plaza-Faverola, A. (2014). Shallow methane hydrate system controls ongoing, downslope sediment transport in a low-velocity active submarine landslide complex, Hikurangi Margin, New Zealand. *Geochem. Geophys. Geosystems* 15, 4137–4156. doi:10.1002/2014GC005379
- Nittrouer, C. A. (1999). Strataform: Overview of its design and synthesis of its results. *Mar. Geol.* 154, 3–12. doi:10.1016/S0025-3227(98)00128-5
- Paull, C. K., Caress, D. W., Thomas, H., Lundsten, E., Anderson, K., Gwiazda, R., et al. (2015). Seafloor geomorphic manifestations of gas venting and shallow subbottom gas hydrate occurrences. *Geosphere* 11, 491–513. doi:10.1130/ges01012.1
- Paull, C. K., Normark, W. R., Ussler, W., Iii, Caress, D. W., and Keaten, R. (2008). Association among active seafloor deformation, mound formation, and gas hydrate growth and accumulation within the seafloor of the Santa Monica Basin, offshore California. *Mar. Geol.* 250, 258–275. doi:10.1016/j.margeo.2008.01.011
- Phrampus, B. J., Harris, R. N., and Tréhu, A. M. (2017). Heat flow bounds over the Cascadia margin derived from bottom simulating reflectors and implications for thermal models of subduction. *Geochem. Geophys. Geosystems* 18, 3309–3326. doi:10.1002/2017gc007077
- Pohlman, J. W., Kaneko, M., Heuer, V. B., Coffin, R. B., and Whiticar, M. (2009). Methane sources and production in the northern Cascadia margin gas hydrate system. *Earth Planet. Sci. Lett.* 287, 504–512. doi:10.1016/j.epsl.2009.08.037
- Prouty, N. G., and Baker, M. C. (2022). *CTD profiles and discrete water-column measurements collected off California and Oregon during NOAA cruise SH-18-12 (USGS field activity 2018-663-FA) from October to November 2018 U.S. Geological Survey Data Release*. doi:10.5066/P99MJ096
- Prouty, N. G., Brothers, D. S., Kluesner, J. W., Barrie, J. V., Andrews, B. D., Lauer, R. M., et al. (2020). Focused fluid flow and methane venting along the Queen Charlotte fault, offshore Alaska (USA) and British Columbia (Canada). *Geosphere* 16, 1336–1357. doi:10.1130/ges02269.1
- Prouty, N. G. (2023). *Geochemistry of authigenic carbonates from Cascadia margin*. U.S. Geological Survey data release. doi:10.5066/P9J10NH5
- Prouty, N. G., Sahy, D., Ruppel, C. D., Roark, E. B., Condon, D., Brooke, S., et al. (2016). Insights into methane dynamics from analysis of authigenic carbonates and chemosynthetic mussels at newly-discovered Atlantic Margin seeps. *Earth Planet. Sci. Lett.* 449, 332–344. doi:10.1016/j.epsl.2016.05.023
- Reed, D. L., Silver, E. A., Tagudin, J. E., Shipley, T. H., and Vrolijk, P. (1990). Relations between mud volcanoes, thrust deformation, slope sedimentation, and gas hydrate, offshore north Panama. *Mar. Petroleum Geol.* 7, 44–54. doi:10.1016/0264-8172(90)90055-L
- Riedel, M., Scherwath, M., Römer, M., Veloso, M., Heesemann, M., and Spence, G. D. (2018). Distributed natural gas venting offshore along the Cascadia margin. *Nat. Commun.* 9, 3264. doi:10.1038/s41467-018-05736-x
- Ruppel, C. D., and Kessler, J. D. (2017). The interaction of climate change and methane hydrates. *Rev. Geophys.* 55, 126–168. doi:10.1002/2016RG000534
- Ruppel, C. D. (2011). Methane hydrates and contemporary climate change. *Nat. Education Knowl.* 2, 12.
- Ruppel, C. D., and Waite, W. F. (2020). Timescales and processes of methane hydrate formation and breakdown, with application to geologic systems. *J. Geophys. Res. Solid Earth* 125, e2018JB016459. doi:10.1029/2018JB016459
- Ryan, W. B. F., Carbotte, S. M., Coplan, J. O., O'hara, S., Melkonian, A., Arko, R., et al. (2009). Global multi-resolution topography synthesis. *Geochem. Geophys. Geosystems* 10. doi:10.1029/2008gc002332
- Saffer, D. M., and Bekins, B. A. (2002). Hydrologic controls on the morphology and mechanics of accretionary wedges. *Geology* 30, 271–274. doi:10.1130/0091-7613(2002)030<0271:hctoma>2.0.co;2
- Saffer, D. M., and Tobin, H. J. (2011). Hydrogeology and mechanics of subduction zone forearcs: Fluid flow and pore pressure. *Annu. Rev. Earth Planet. Sci.* 39, 157–186. doi:10.1146/annurev-earth-040610-133408
- Sahling, H., Masson, D. G., Ranero, C. R., Hühnerbach, V., Weinrebe, W., Klauke, I., et al. (2008). Fluid seepage at the continental margin offshore Costa Rica and southern Nicaragua. *Geochem. Geophys. Geosystems* 9. doi:10.1029/2008GC001978
- Shapiro, S. S., and Wilk, M. B. (1965). An analysis of variance test for normality (complete samples). *Biometrika* 52 (3–4), 591–611. doi:10.1093/biomet/52.3-4.591
- Silver, E. A. (1972). Pleistocene tectonic accretion of the continental slope off Washington. *Mar. Geol.* 13, 239–249. doi:10.1016/0025-3227(72)90053-9
- Skarke, A., Ruppel, C., Kodis, M., Brothers, D., and Lobecker, E. (2014). Widespread methane leakage from the sea floor on the northern US Atlantic margin. *Nat. Geosci.* 7, 657–661. doi:10.1038/ngeo2232
- Sommerfield, C. K., and Nittrouer, C. A. (1999). Modern accumulation rates and a sediment budget for the Eel shelf: A flood-dominated depositional environment. *Mar. Geol.* 154, 227–241. doi:10.1016/S0025-3227(98)00115-7
- Suess, E. (2014). Marine cold seeps and their manifestations: Geological control, biogeochemical criteria and environmental conditions. *Int. J. Earth Sci.* 103, 1889–1916. doi:10.1007/s00531-014-1010-0
- Suess, E., Torres, M. E., Bohrmann, G., Collier, R. W., Greinert, J., Linke, P., et al. (1999). Gas hydrate destabilization: Enhanced dewatering, benthic material turnover and large methane plumes at the Cascadia convergent margin. *Earth Planet. Sci. Lett.* 170, 1–15. doi:10.1016/S0012-821X(99)00092-8
- Teichert, B. M. A., Eisenhauer, A., Bohrmann, G., Haase-Schramm, A., Bock, B., and Linke, P. (2003). U/Th systematics and ages of authigenic carbonates from Hydrate

- Ridge, Cascadia margin: Recorders of fluid flow variations. *Geochimica Cosmochimica Acta* 67, 3845–3857. doi:10.1016/S0016-7037(03)00128-5
- Teichert, B. M. A., Torres, M. E., Bohrmann, G., and Eisenhauer, A. (2005). Fluid sources, fluid pathways and diagenetic reactions across an accretionary prism revealed by Sr and B geochemistry. *Earth Planet. Sci. Lett.* 239, 106–121. doi:10.1016/j.epsl.2005.08.002
- Torres, M. E., Embley, R. W., Merle, S. G., Tréhu, A. M., Collier, R. W., Suess, E., et al. (2009). Methane sources feeding cold seeps on the shelf and upper continental slope off central Oregon, USA. *Geochem. Geophys. Geosystems* 10. doi:10.1029/2009GC002518
- Torres, M. E., Teichert, B. M. A., Tréhu, A. M., Borowski, W., and Tomaru, H. (2004). Relationship of pore water freshening to accretionary processes in the Cascadia margin: Fluid sources and gas hydrate abundance. *Geophys. Res. Lett.* 31. doi:10.1029/2004GL021219
- Torres, M. E., Tréhu, A. M., Cespedes, N., Kastner, M., Wortmann, U. G., Kim, J. H., et al. (2008). Methane hydrate formation in turbidite sediments of northern Cascadia, IODP Expedition 311. *Earth Planet. Sci. Lett.* 271, 170–180. doi:10.1016/j.epsl.2008.03.061
- Tréhu, A. M., Blakely, R. J., and Williams, M. C. (2012). Subducted seamounts and recent earthquakes beneath the central Cascadia forearc. *Geology* 40, 103–106. doi:10.1130/g32460.1
- Trehu, A. M., Lin, G., Maxwell, E., and Goldfinger, C. (1995). A seismic reflection profile across the Cascadia subduction zone offshore central Oregon: New constraints on methane distribution and crustal structure. *J. Geophys. Res. Solid Earth* 100, 15101–15116. doi:10.1029/95jb00240
- Tréhu, A. M., Long, P. E., Torres, M. E., Bohrmann, G., Rack, F. R., Collett, T. S., et al. (2004). Three-dimensional distribution of gas hydrate beneath southern Hydrate Ridge: Constraints from ODP leg 204. *Earth Planet. Sci. Lett.* 222, 845–862. doi:10.1016/j.epsl.2004.03.035
- Tréhu, A. M., and Phrampus, B. J. (2022). “Accretionary wedge tectonics and gas hydrate distribution in the Cascadia forearc,” in *World atlas of submarine gas hydrates in continental margins*. Editors J. Mienert, C. Berndt, A. M. Tréhu, A. Camerlenghi, and C.-S. Liu (Cham: Springer International Publishing), 121–130.
- Tréhu, A. M., Torres, M. E., Moore, G. F., Suess, E., and Bohrmann, G. (1999). Temporal and spatial evolution of a gas hydrate-bearing accretionary ridge on the Oregon continental margin. *Geology* 27, 939–942. doi:10.1130/0091-7613(1999)027<0939:taseoa>2.3.co;2
- Triezenberg, P. J., Hart, P. E., and Childs, J. R. (2016). *National archive of marine seismic surveys (namss): A United States geological survey data website of marine seismic reflection data within the us exclusive economic zone (eez)*. U.S. Geological Survey Data Release. doi:10.5066/F7930R7P
- Von Huene, R., and Scholl, D. W. (1991). Observations at convergent margins concerning sediment subduction, subduction erosion, and the growth of continental crust. *Rev. Geophys.* 29, 279–316. doi:10.1029/91RG00969
- Walton, M. a. L., Staisch, L. M., Dura, T., Pearl, J. K., Sherrod, B., Gomberg, J., et al. (2021). Toward an integrative geological and geophysical view of Cascadia subduction zone earthquakes. *Annu. Rev. Earth Planet. Sci.* 49, 367–398. doi:10.1146/annurev-earth-071620-065605
- Watson, S. J., Mountjoy, J. J., Barnes, P. M., Crutchley, G. J., Lamarche, G., Higgs, B., et al. (2020). Focused fluid seepage related to variations in accretionary wedge structure, Hikurangi margin, New Zealand. *Geology* 48, 56–61. doi:10.1130/G46666.1
- Watt, J. T., and Brothers, D. S. (2020). Systematic characterization of morphotectonic variability along the Cascadia convergent margin: Implications for shallow megathrust behavior and tsunami hazards. *Geosphere* 17, 95–117. doi:10.1130/ges02178.1
- Wells, R. E., Blakely, R. J., and Weaver, C. S. (2002). “Cascadia microplate models and within-slab earthquake,” in *The Cascadia subduction zone and related subduction systems: U.S. Geological survey open-file report 02-328 and geological survey of Canada open-file 4350*. Editors S. Kirby, K. Wang, and S. Dunlop, 17–23. doi:10.3133/ofr02328
- Westbrook, G. K., Thatcher, K. E., Rohling, E. J., Piotrowski, A. M., Pälike, H., Osborne, A. H., et al. (2009). Escape of methane gas from the seabed along the West Spitsbergen continental margin. *Geophys. Res. Lett.* 36. doi:10.1029/2009GL039191
- Wilk, M. B., and Gnanadesikan, R. (1968). Probability plotting methods for the analysis of data. *Biometrika* 55 (1), 1–17. doi:10.2307/2334448
- Wood, W. T., Hart, P. E., Hutchinson, D. R., Dutta, N., Snyder, F., Coffin, R. B., et al. (2008). Gas and gas hydrate distribution around seafloor seeps in Mississippi Canyon, Northern Gulf of Mexico, using multi-resolution seismic imagery. *Mar. Petroleum Geol.* 25, 952–959. doi:10.1016/j.marpetgeo.2008.01.015